Reflection for Subwavelength Annular Mode in Metals

by

Dan Li
B.Sc., Peking University, 2007

A Thesis Submitted in Partial Fulfillment of the
Requirements for the Degree of

MASTER OF APPLIED SCIENCE

in the Department of Electrical and Computer Engineering

Reflection for Subwavelength Annular Mode in Metals

by

Dan Li
B.Sc., Peking University, 2007

Supervisory Committee

Dr. R. Gordon, Supervisor
(Department of Electrical and Computer Engineering)

Dr. Jens Bornemann, Departmental Member
(Department of Electrical and Computer Engineering)

Supervisory Committee

Dr. R. Gordon, Supervisor
(Department of Electrical and Computer Engineering)

Dr. Jens Bornemann, Departmental Member
(Department of Electrical and Computer Engineering)

ABSTRACT

The coaxial aperture structure has been under intensive study in recent years, particularly since it exhibits electromagnetic transmission resonances that are stronger than its circular aperture counterpart. In our work, we study the resonance properties of a coaxial aperture in a perfect electric conductor (PEC) and in a real metal. For PEC, The dielectric constant is infinite and for real metal the dielectric constant is finite. We develop theory for reflection phase and amplitude in coaxial aperture at the end of a metal plate. While most of the past works of coaxial aperture focused on the propagation of light within the aperture structure and ignore the reflection at end-face,we find that the rection properties at the end-face are critical to determine both the wavelength and quality of Fabry-Perot resonant transmission of coaxial structure. Finite-difference time-domain calculations agree well with our theory. We first consider the PEC case, and later to develop the theory to account for real metal case. In real metal, the phase and amplitude of reflection are quantitatively different from PEC because of plasmonic effects. Such difference arises from the new physics associated with surface plasmons. This work is of interest to ongoing studies of coaxial structures in metal films, which could impact many fields including filter effect, optical sensing, optical trapping, near-field spectroscopy and metamaterials.

Contents

Supervisory Committee **ii**

Abstract **iii**

Table of Contents **iv**

List of Tables **vi**

List of Figures **vii**

List of Acronyms **xi**

Acknowledgements **xii**

Dedication **xiv**

1 General Introduction **1**

1.1 Outline of the Thesis 3

2 Background **4**

2.1 Coaxial Modes in a Perfect Electric Conductor 4

2.2 Review of Maxwell's Equations in Media 6

2.3 Basic Theory of Plasmons 7

2.3.1 Surface Plasmons and Dispersion Relation 7

2.3.2 Cylindrical Surface Plasmons 9

2.4 Mode Matching Method 12

2.5 Single Mode Matching 15

2.6 Aperture Theory and Extraordinary Optical Transmission 16

2.6.1 Recent Developments in Transmission Through Apertures . . 16

2.7 Summary 19

3 Finite-difference Time-domain **20**
3.1 Theory of Finite-difference Time-domain 20
3.2 Work Using FDTD Simulations 25
3.2.1 Lumerical FDTD Solutions 25
3.2.2 MEEP 26

4 Electromagnetic transmission resonances for a single annular aperture in a metal plate **31**
4.1 Introduction 31
4.2 Theory of Reflection at the End of an Annular Aperture 31
4.3 Fabry-Perot Resonances of Coax in Metal Slab 34
4.4 Conclusion 39

5 Tuning Plasmonic Resonance of an Annular Aperture in Metal Plate **41**
5.1 Introduction 41
5.2 Theory of end-face reflection from an annular aperture in a metal plate 41
5.3 Behavior of reflection coefficient 44
5.4 Fabry-Perot Resonances 45
5.5 Conclusion 50

6 Conclusions and Future Work **53**
6.1 Summarization of our Findings 53
6.2 Applications of Coaxial Geometry 53
6.2.1 Filter Effect 53
6.2.2 Near Field Optics 54
6.2.3 Single annular aperture in sensors 55
6.2.4 Negative-index Metamaterials 55

Bibliography **58**

A Additional Information **64**
A.1 MEEP Code 64
A.2 MAPLE Code 65

List of Tables

Table 5.1 The effective refractive indexes and peak wavelength for geometries in Fig. 5.3, for structures designed to have peak at 632.8 nm. 49

List of Figures

Figure 2.1 The surface plasmon in metal-dielectric interface (shown the $x-z$ plane). The gray stands for metal and yellow for dielectric [1]. . 8
Figure 2.2 The dispersion relation of surface plasmons for different material are different [1]. 10
Figure 2.3 Schematic view of an coaxial aperture. The regions 1, 2, 3 and 4 has relative permittivity of ϵ_1, ϵ_2, ϵ_3 and ϵ_4 respectively. . . . 11
Figure 2.4 The coaxial aperture with inner radius a, outer radius b and length l is terminated at the right end ($z = 0$ plane), where a dielectric material with permittivity ϵ'_d extends to $\rho = c$ far. . . 14
Figure 2.5 Past work using mode matching method. (a) The single slit [2] (b) Angle-dependent incidence of single slit [3] (c) The double slits [4] (d) Cylindrical nanorod [5]. All the slits are subwavelength dimensions. 17

Figure 3.1 Three-dimensional FDTD lattics, the gray region applies to the two-dimensional lattice [6]. In a unit cell of the lattice, every $\mathbf{E}(\mathbf{H})$ component is centered in space and surrounded by four circulating $\mathbf{H}(\mathbf{E})$ components, simulating both the differential and integral forms of Maxwell's equations. 21
Figure 3.2 Field components are also centered in time, in a leapfrog pattern in the t-z plane. 22
Figure 3.3 Figures show the finite size PMLs, the outer PECs/PMCs and choices of loss terms. 24

Figure 3.4 The geometry we setup to simulate our coaxial structure using Lumerical FDTD solutions. The right up one is the perspective view. The left up one is the top view. The lower two are side views. The dipole source is along the z-direction. The symmetry along x-axis and y-axis is used to reduce the computation domain to a quarter. 27

Figure 3.5 Dielectric function (black = high, white = air),for the coaxial structure with $a = 100$ nm, $b = 120$ nm. 28

Figure 3.6 Transmission spectral of the coaxial structure from MEEP. The geometry is the same as in Fig. 3.5. Convergence is ensured by increasing the resolution and reducing the cell size. 29

Figure 3.7 The same geometry as in Fig. 3.5. Blue curve: simulated by MEEP, with resolution 550 and cell size 2. Red curve: simulated by Lumerical FDTD Solutions. The plane wave source is at $z = -500$ nm. 30

Figure 4.1 Schematic of annular aperture in a metal plate (i.e., a coaxial aperture). The electric field polarization of the TEM mode is also shown. 32

Figure 4.2 Electromagnetic transmission of a z-polarized dipole source and at distance $0.5b$ from the plate as measured through coaxial aperture, as calculated by FDTD. $a = 0.9b, b = l$. Normalized to the same source with a semi-infinite metal plate. Triangles show the frequency of resonances predicted by the analytic theory and using Eq. (4.12). Dotted vertical lines at frequency of 0.5, 1, 1.5, 2 and 2.5 c/b show the position of the resonances when neglecting the phase of reflection. 35

Figure 4.3 Left: the simulated structure is surrounded by PML (not shown in the picture). The monitor is positioned at the right end surface ($z = 0$ plane). Right: the infinitely long coaxial structure is used to normalize the transmission. PML cuts through the coax structure at far field. The monitor is also positioned at $z = 0$ plane. 37

Figure 4.4 Left: the simulated structure is surrounded by PML (not shown in the picture). The monitor is positioned at the right end surface ($z = 0$ plane). Right: the infinitely long coaxial structure is used to normalize the transmission. PML cuts through the coax structure at far field. The monitor is also positioned at $z = 0$ plane. 38

Figure 4.5 (a) Amplitude of reflection extracted from FDTD calculated transmission for $l = 4b$ and $a = 0.9b$, as compared with reflection calculated from the analytic theory of Eqs. (4.10) and (4.11). (b) Phase of reflection calculated by the analytic theory for $a = 0.9b$, showing oscillations. 40

Figure 5.1 Evaluation of the theoretical reflection expression (Eq. 12) for annular apertures in gold plate at 632.8 nm free-space wavelength. The results are contrasted with PEC case in dashed lines. (a) the reflectivity and (b) phase of the reflection coefficient as function of inner radius, a, for slit widths $(b - a)$ of 20 nm and 50 nm. 46

Figure 5.2 Difference between PEC case and real metal for annular aperture with slit size of 20 nm illuminated with 500 nm wavelength light. (a) reflectivity (b)phase. 47

Figure 5.3 (a) Transmission in arbitrary units for $(b - a)$ value of 20 nm. Each curve relates to a different structure as specified in the legend and the dashed line is at 632.8 nm. In this figure a is the inner radius and l is the thickness of the plate (b) The $(b - a)$ value has been changed to 50 nm. 48

Figure 5.4 Variations of resonance wavelength with plate thickness l. The annular aperture inner radius is kept fixed at $a = 50$ nm. 50

Figure 5.5 Electric-field plot in $2D$, calculated by FDTD. The figure shows the cross section of the annular aperture. (a) E-field at the resonance wavelength 632.8 nm (b) E-field at 500 nm wavelength. The scalar bar is shown on the right. 52

Figure 6.1 Schematic and SEM image of the EOT near-field fiber probe. (a) The fiber is tapered and then coated with an aluminum layer to prevent light leakage. The final taper diameter d_t determines the resonant TM mode cutoff-wavelength, by focused ion beam (FIB) milling. The aperture with diameter d_a is milled into a gold layer that is evaporated onto the end face. Inset: Conventional NSOM fiber. (b) The SEM image shows the final configuration with an aperture of diameter $d_a = 110nm$. The scale bar is $500nm$. The figure is from [7] 54

Figure 6.2 Scanning electron microscope image of the coaxial aperture in gold film taken from the FIB. The inner radius is 155 nm and outer radius is 185 nm. A: topview; B: 52° sideview. 56

Figure 6.3 Negative-index metamaterial geometry (from [8]). a, Single-layer NIM slab consisting of a hexagonal array of subwavelength coaxial waveguide structures. The inner radius r_1, outer radius r_2 and array pitch p are defined in the image. b, Unit cell of the periodic structure. The angle-of-incidence θ is shown, as well as the in-plane ($p-$) and out-of-plane ($s-$) polarization directions associated with the incident wavevector k. 57

List of Acronyms

PEC Perfect Electric Concuctor

TEM Transverse Electromagnetic Waves

FP Fabry-Perot

TE Transverse Electric

TM Transverse Magnatic

CSP Cylindrical Surface Plasmons

PML Perfect Matched Layer

FDTD Finite-Difference Time-Domain

AAA Annular Aperture Array

NSOM Near-Spectrum Optical Microscopy

Real Metal the Dielectric Constant is Finite

PEC The Dielectric Constant is Infinite

EOT Extraordinary Optical Transmission

BCs Boundary Conditions

ACKNOWLEDGEMENTS

This thesis will never get to be finished without the help and support from many people. I would like to start by acknowledging a few people in particular. I would like to thank:

Xi and my parents, you are always there whatever comes.

Doctor Gordon, thank you for your mentoring, support, encouragement and patience. Thank you for leading me into the interesting and promising realm of nanoplasmonics. Your patient guidance in my project on re ection for subwavelength coaxial modes is the pivotal step to the completion of this thesis. You are always tireless and meticulous when helping me when helping me on the course study, on the difficulties I encountered in research, and even on the improvement of my technical writing skills. However, the most I benefit from you is that, you have really changed my life. You are always energetic, aggressive and hard-working. Your high sense of responsibility, your d̈o it now" attitude and the care for students will always enlighten me.

Doctor Jens Bornemann, it's my honor to have you as my Supervisory Committee member. Thank you for your time and energy to attend my defense even when you are really having a busy time. I first met you in the course of Antenna and Propagation. I had difficulties with the course project of F̈DTD analysis of antenna" and you were so kind and patient throughout the hard time when I worked on it. Besides contact during the course, you are also concerned about my health, my study in other courses, and my future. Thanks for all your help throughout my graduate study.

Barmak, it was such an fruitful and colorful cooperation experience with you on the project of T̈he plasmonic resonance of coaxial aperture in Real metal case". Thank you for your great contribution of the theory part in Chapter 5.

Doctors Tao Lu and Chris Papadopoulos, it's you who supported me and encouraged me when I first came to Victoria. I am so lucky to have you when I was not in good health condition.

Yuanjie, Aftab, John, Mandira, Ghazal, Lan, Gaby, Ishita, Vincent, and Asif, you guys are really great coworkers and friends. I enjoy the warm atmosphere in the lab with you guys, and of course also the happy moments hanging

out together. You make my research in the lab, and my life in Victoria more enriched and happier. Yuanjie and Aftab, you are so patient to help me solve all kinds of problems with my course and research. John, there are lots of laughters as long as being with you. I like to play badminton and dine out with you. Ghazal, Mandira, Lan, Gaby and Ishita, you are all really very sweet girls, I do like to time being with you. All the people in our Nanoplasmonics lab have made my life in Victoria more colorful and meaningful. Thank you for your companionship!

Xiao Pingping, Xiao Yangyang, Xiao Yuanyuan, Haiying, Congzhi, Da Shixiong, Er Shixiong, and Sha Shidi, the friendship with you made all the difference during these two years. It is the most precious treasure of my life.

Vicky Smith, Moneca Bracken, Lynn Barrett, Janice Closson, and Eric Laxdal, you help me with all these important, but numerous and trivial stu during my graduate study. Thank you for your kindness and care.

NSERC and University of Victoria, Lastly, I would like to acknowledge National Science and Engineering Research Council and the University of Victoria for providing financial support in the form of a research grant and a university fellowship, respectively. The support definitely helped me resolve the

nancial burden pertaining to my studies.

I believe I know the only cure, which is to make one's centre of life inside of one's self, not selfishly or excludingly, but with a kind of unassailable serenity-to decorate one's inner house so richly that one is content there, glad to welcome any one who wants to come and stay, but happy all the same in the hours when one is inevitably alone.

Edith Wharton

DEDICATION

To Xi and my parents, whom I love and who love me.

Chapter 1

General Introduction

Since the discovery of extraordinary optical transmission (EOT) in 1998 [9], there has been an explosion of research on the transmission through subwavelength apertures in metal films. The shape of the aperture plays an important role in the transmission characteristics [10, 11, 12]. The coaxial (annular) shape is particularly interesting because it has modes with long cutoff wavelengths inside the aperture [13, 10], which underlies theoretical predictions and experimental demonstrations of increased transmission for coaxial aperture arrays [10, 14, 15, 16, 17, 18, 19, 20].

At visible-infrared wavelengths, a recent work has demonstrated EOT through a single coaxial aperture by exciting the lowest order mode that is radially-polarized [21]. At microwave frequencies, Fabry-Perot transmission resonances have been observed from that radially-polarized mode for off-axis excitation, as required by symmetry [22]. For a perfect electric conductor (PEC), which can reasonably approximate the behavior of metals at longer wavelengths, that lowest order radially polarized mode is transverse electromagnetic (TEM), which has the interesting properties of having no cutoff and of having the same wavevector as a plane-wave in free-space. The TEM mode can propagate in annular apertures of infinitesimal dimension, which is interesting for extreme subwavelength coupling.

As pointed out previously [22], there are many similarities between the annular aperture and a linear slit, since the annular aperture can be thought of as a slit bent around to join on itself. For the linear slit, a theoretical work has shown that the lowest order TEM mode will give Fabry-Perot transmission resonances [23]. The key contribution of that work was to show that slit width is critical to the phase and amplitude of reflection, which changes the frequency and quality of the transmission resonances. Similarly for annular apertures, the phase and amplitude of reflection

play a vital role in determining the properties of the resonances, as will be described in this work. Unlike a slit, however, the coaxial aperture shows transverse resonances.

Coaxial waveguides are used extensively at the microwave frequencies because they support a propagating TEM mode for infinitesimal dimensions. For visible and infrared frequencies, the situation changes and there has been considerable effort to understand the influence of surface plasmons within cylindrical coaxial waveguides and geometries [24, 16, 21, 25, 9, 26, 27, 5, 17, 28]. The cylindrical surface plasmon (CSP) can extend the cut-off of the waveguide modes for narrow gaps between the metal sides. As it will be shown, the Bessel field profile of CSP can have rapid decay in metal and free space, with sharp localization at metal boundaries. In this regard, phenomena such as extraordinary optical transmission requires consideration of the localized resonances associated with the CSP, which have shown to play an important role, both theoretically and experimentally [16, 29, 30, 19, 31, 32, 18]. The properties of CSPs have been of interest to a wide range of applications including: nonlinear optics [16, 17], metamaterials [8, 33], THz waveguiding [34], sub-wavelength and near-field optics [35, 28, 27, 36, 37, 38, 39], and band-pass filters [40, 13].

While past works focused on the propagation of light within the aperture structure, the reflection properties at the end-face are critical to determine both the wavelength and quality of Fabry-Perot resonant transmission from the CSP. The phase of reflection associated with the end-faces of a coaxial aperture affect the Fabry-Perot resonances seen at the microwave frequencies [22].

It is common in the literature to first consider the PEC case as simplified theory that accounts for the geometric optical physics, and later to develop a more detailed theory to account for the plasmonic influence. For example, the progression of study on the single slit problem has followed that trend. An early work to account for the phase and amplitude of reflection for a single slit in a metal concentrated on the PEC case, showing significant geometric influence on the phase of reflection [23]. Following that work, the effects associated with the finite conductance of the metal were shown to dominate the resonances in the microwave regime [41]. For real metals in the visible-IR regime, later theories revealed the plasmonic influences on the reflection properties [2] and the ability to generate surface plasmons at the slit [42]. In each of these works, new physics was uncovered when accounting for the real response of the metal.

1.1 Outline of the Thesis

In this work, I follow the same approach, first solving the PEC case, then investigating the real metal case. Parts of the work in the thesis has been published in [43, 44, 45].

Chapter 2 presents the background and basic theory of extraordinary optical EOT. The former work about EOT is generally summarized.

Chapter 3 presents the finite-difference time-domain (FDTD).

Chapter 4 presents for the reflection phase and amplitude of the lowest order TEM mode in a single coaxial aperture at the end of a metal plate. The resonance frequency can also be influenced by the phase of reflection [5], not as thought only determined by the geometry [23]. Both the phase and amplitude of reflection are critical in the design of coaxial apertures in metal plates. The FDTD simulations of the propagation of light is presented.

In chapter 5, we present a theory for the reflection phase and amplitude of coaxial apertures when embedded in real metal.

Chapter 6 presents the conclusion, potential applications in advancing near field optics, sensors and metamaterials [33, 8], and future work.

Chapter 2

Background

The coaxial modes we studied in this work are found using Maxwell's equations. It is useful to start this chapter by reviewing Maxwell's equations. Although the coax reflection does not require surface plasmons, when considering real metal case, plasmon effects have to be accounted for. Therefore, we introduce concepts of surface plasmons and cylindrical surface plasmons. The analytical approach we develop is based on the mode matching method (MMM). I give an example of discontinuity of coaxial waveguide to elucidate MMM, as well as mode orthogonality, expansion and normalization.

2.1 Coaxial Modes in a Perfect Electric Conductor

Since we are interested in a coax-free space boundary, it is useful to know the modes. First for a PEC, the fields of the coaxial structure as depicted in 4.1 can be derived from a scalar potential function $\Phi(\rho, \phi)$ [46].

$$\frac{1}{\rho}\frac{\partial}{\partial\rho}(\rho\frac{\partial\Phi(\rho,\phi)}{\partial\phi}) + \frac{1}{\rho^2}\frac{\partial^2\Phi(\rho,\phi)}{\partial\phi^2} = 0 \tag{2.1}$$

where we use cylindrical co-ordinates for our structure: the axis of the coax is along the $z-$ axis, ρ is the radial axis and ϕ is the azimuth direction. The inner and outer radius of the coaxial structure is a and b, respectively.

This equation can be solved using the boundary conditions:

$$\Phi(a, \phi) = 0, \qquad \Phi(b, \phi) = 0 \tag{2.2}$$

And the explicit expression of the solutions is as:

$$E_\rho = \frac{e^{ik_d z}}{\rho}, \tag{2.3}$$

$$H_\phi = \sqrt{\frac{\epsilon_d \epsilon_0}{\mu_0}} \frac{e^{ik_d z}}{\rho}, \tag{2.4}$$

where $k_d = \omega\sqrt{\mu_0 \epsilon_0 \epsilon_d}$, ω is the angular frequency, ϵ_d is the permittivity of dielectric inside the aperture of the coax, and ϵ_0 and μ_0 are the free-space permittivity and permeability.

Besides TEM modes as described in Chapter 3, the coaxial aperture can also support TE and TM modes, which are usually cut-off for extremely small apertures. The TE_{11} mode is the dominant mode for linear polarization excitation, so it is of primary importance. The transmission of TE_{11} mode is left as the future work.

For TE modes, $E_z = 0$, and the H_z satisfies the wave equation:

$$\left\{ \frac{\partial^2}{\partial \rho^2} + \frac{1}{\rho}\frac{\partial}{\partial \rho} + \frac{1}{\rho^2}\frac{\partial^2}{\partial \phi^2} + k_c^2 \right\} h_z(\rho, \phi) = 0 \tag{2.5}$$

where $H_z(\rho, \phi, z) = h_z(\rho, \phi) e^{-j\beta z}$, $k_c = k^2 - \beta^2$. The general solution to this equation is as:

$$h_z(\rho, \phi) = (Asin(n\phi) + Bcos(n\phi))(CJ_n(k_c\rho) + DY_n(k_c\rho)) \tag{2.6}$$

The boundary conditions are

$$E_\phi(\rho, \phi) = 0 \qquad for \quad \rho = a, \quad b. \tag{2.7}$$

Therefore E_ϕ can be expressed as:

$$E_\phi = \frac{j\omega\mu}{k_c}(Asin(n\phi) + Bcos(n\phi))(CJ_n'(k_c\rho) + DY_n'(k_c\rho))e^{-j\beta z} \tag{2.8}$$

Thus the boundary conditions are specified as:

$$(CJ_n'(k_c a) + DY_n'(k_c a)) = 0 \tag{2.9}$$

$$(CJ'_n(k_c b) + DY'_n(k_c b)) = 0 \tag{2.10}$$

2.2 Review of Maxwell's Equations in Media

The equations governing electromagnetic phenomena are the Maxwell's equations. Their four differential forms are written below in SI units.
Gauss' Law (electric):

$$\nabla \cdot \vec{D} = \rho_e \tag{2.11}$$

Gauss's Law (magnetic):

$$\nabla \cdot \vec{B} = 0 \tag{2.12}$$

Maxwell-Faraday Equation:

$$\nabla \times \vec{E} = -\frac{\partial \vec{B}}{\partial t} \tag{2.13}$$

Maxwell-Ampere Equation:

$$\nabla \times \vec{B} = \vec{J} + \frac{\partial \vec{D}}{\partial t} \tag{2.14}$$

where ∇ is the vectorial differential operator, $\vec{D}$ is the electric displacement vector, ρ_e is the electric charge density, $\vec{B}$ is the magnetic flux density, $\vec{E}$ is the electric field, $\vec{J}$ is the charge current density and $\vec{H}$ is the magnetic field. Considering a source free, lossless medium with a scalar dielectric constant ϵ and a scalar magnetic permeability μ, the constitutive relations are simple:

$$\vec{D} = \epsilon \vec{E}, \tag{2.15}$$

$$\vec{B} = \mu \vec{H}, \tag{2.16}$$

Substituting in the constitutive relations, the Maxwell's equations can be expressed as:

$$\nabla \times \vec{E} = -j\omega\mu\vec{H}, \tag{2.17}$$

$$\nabla \times \vec{H} = j\omega\epsilon\vec{E}. \tag{2.18}$$

where $j = \sqrt{-1}$ and ω is the frequency.

These equations are explicitly solved when applying boundary conditions at the interface of two different media: the displacement vector and magnetic flux density are continuous normal to the boundary, and the tangential components of electric and magnetic fields are also continuous at the boundary. To clarify, we express the boundary conditions as follows:

$$(\hat{D}_1 - \hat{D}_2) \cdot \hat{n} = 0 \tag{2.19}$$

$$(\hat{B}_1 - \hat{B}_2) \cdot \hat{n} = 0 \tag{2.20}$$

$$(\hat{D}_1 - \hat{D}_2) \times \hat{n} = 0 \tag{2.21}$$

$$(\hat{B}_1 - \hat{B}_2) \times \hat{n} = 0 \tag{2.22}$$

where $\hat{n}$ is boundary surface normal. These boundary conditions are derived in the absence of surface charges and surface currents.

2.3 Basic Theory of Plasmons

2.3.1 Surface Plasmons and Dispersion Relation

Surface plasmons are electron density waves at the surface of a metal. Above the plasma frequency, metals become transparent as they allow for EM wave propagation. There are bulk plasmons and surface plasmons (SPs), and the latter can exist at the interface between any two materials where the real part of the dielectric function have different signs across the interface (e.g. a metal-dielectric interface, such as a metal plate in air). Fig 2.1 depicts SPs at metal-dielectric interface. The strong localization of electromagnetic waves are shown in the red arrows.

The Drude metal model is used to describe the electronic response of materials. Considering the conduction electrons with damping, the equation of motion is:

$$m\frac{d^2x}{dt^2} + m\gamma\frac{dx}{dt} = eE_0e^{i\omega t} \tag{2.23}$$

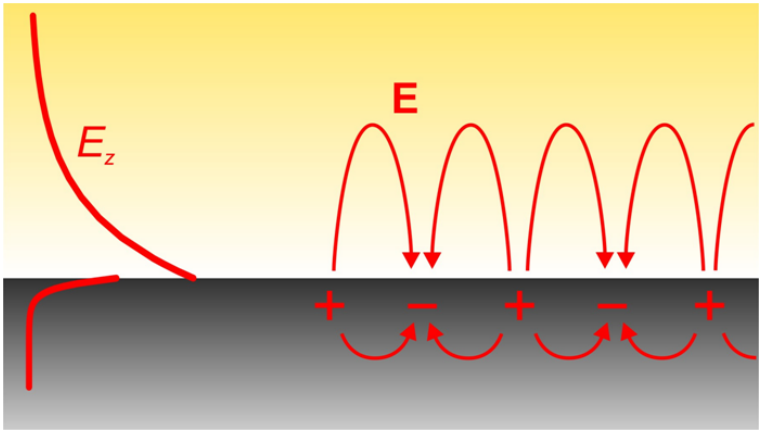

Figure 2.1: The surface plasmon in metal-dielectric interface (shown the $x-z$ plane). The gray stands for metal and yellow for dielectric [1].

Therefore,

$$\epsilon = 1 + \frac{Nex}{\epsilon_0 E} = 1 - \frac{\omega_P^2}{\omega^2 - i\omega\gamma} \tag{2.24}$$

with collision frequency γ and plasma frequency:

$$\omega_P \equiv \sqrt{\frac{Ne^2}{m\epsilon_0}}, (when \quad \gamma \ll \omega_P) \tag{2.25}$$

For modified Drude model, the contribution of background response is considered, thus:

$$\epsilon' = \epsilon_b - \frac{\omega_P^2}{\omega^2}, \quad \epsilon'' = \frac{\omega_P^2}{\omega^3}\gamma \tag{2.26}$$

For practical purposes, a big advantage of the Drude model is that it can easily be incorporated into time-domain based numerical solvers for Maxwells equations, such as the FDTD scheme, via the direct calculation of the induced currents using:

$$m\boldsymbol{x} + m\gamma\boldsymbol{x} = -e\boldsymbol{E}e^{-i\omega t} \tag{2.27}$$

The EM waves at metal-dielectric interface can be written as:

$$\vec{E}_d(x,z,t) = \vec{E}_{d,0}e^{i(k_x x + k_z z - \omega t)}, \quad \vec{E}_m(x,z,t) = \vec{E}_{m,0}e^{i(k_x x - k_z z - \omega t)} \tag{2.28}$$

Substituting EM wave into wave equation, we get:

$$\nabla^2 \vec{E}_{d,m} = \mu_0\mu_{d,m}\epsilon_0\epsilon_{d,m}\frac{\partial^2 \vec{E}_{d,m}}{\partial t^2} \tag{2.29}$$

Also the boundary conditions are used: $E_{\|}$ and $H_{\|}$ across boundary are continuous:

$$E_{x,m} = E_{x,d}, \quad H_{y,m} = H_{y,d} \tag{2.30}$$

Then we can get the dispersion relations:
in the $x-$direction:

$$k_x = k'_x + ik''_x = \frac{\omega}{c}\Big\{\frac{\epsilon_m \epsilon_d}{\epsilon_m + \epsilon_d}\Big\}^{\frac{1}{2}} \tag{2.31}$$

in the $z-$direction:

$$k_{z,m} = k'_{z,m} + ik''_{z,m} = \frac{\omega}{c}\Big\{\frac{\epsilon_m^2}{\epsilon_m + \epsilon_d}\Big\}^{\frac{1}{2}} \tag{2.32}$$

When $\epsilon_m = -\epsilon_d$, we have the plasma frequency $\omega_{SP} = \omega$.

Therefore, the Drude model describes the typical metal response as [47]:

$$\epsilon_m = \epsilon_0[1 - \frac{\omega_P^2}{\omega^2 - j\nu\omega}] = \epsilon_0[1 - \frac{\omega_P^2}{\omega^2 + \nu^2} - j\frac{\omega_P^2 \nu}{\omega(\omega^2 + \nu^2)}], \tag{2.33}$$

where ω is the excitation frequency, ν is the effective electron collision frequency, and ω_P is the bulk electron plasma frequency.

At optical wavelength, $\omega^2 + \nu^2 < \omega_P^2$, the real part of ϵ_m is negative, with the real part of surrounding dielectric material being positive, which cause the existence of SPP wave. Fig. 2.1 shows the strong localization of the EM field at the metal and dielectric interface.

$$k_{SP} = \frac{\omega}{c}\sqrt{\frac{\epsilon_m \epsilon_d}{\epsilon_m + \epsilon_d}}, \tag{2.34}$$

Eq. 2.34 is the dispersion relation for surface plasmons.

2.3.2 Cylindrical Surface Plasmons

Fig. 2.3shows a schematic of the geometry under consideration. An coaxial aperture in a metal film is coaxial with the z-axis within the cylindrical coordinate system (ρ, ϕ, z) , and the end-face of the metal terminates at $z = 0$. Considering only the lowest-order TM mode (CSP) [47], the field at $z = 0^-$ can be expressed as:

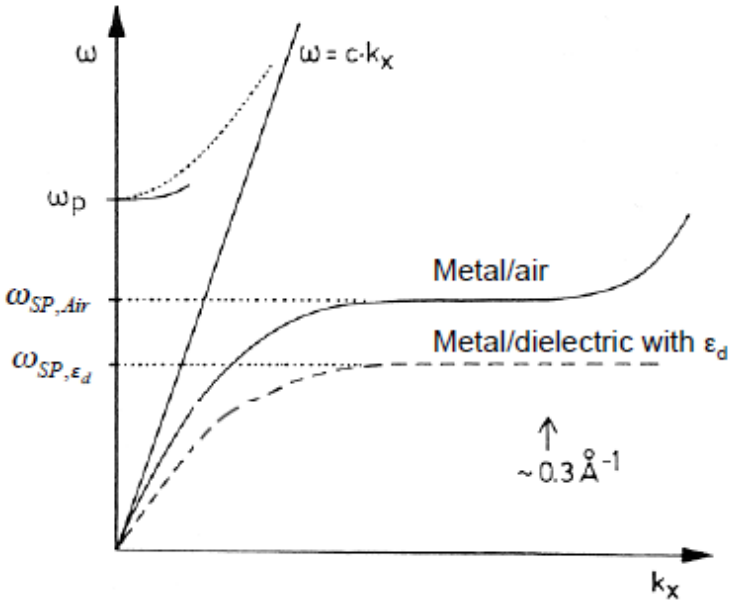

Figure 2.2: The dispersion relation of surface plasmons for different material are different [1].

$$E_\rho(\rho,\phi,z=0^-) \approx \begin{cases} E_\rho^{(1)} &= (1+r)\frac{-j\beta}{p_1}A_1 I_1(p_1\rho) & \text{if } \rho < a \\ E_\rho^{(2)} &= (1+r)\frac{-j\beta}{p_2}[A_2 I_1(p_2\rho) - A_3 K_1(p_2\rho)] & \text{if } a<\rho<b \\ E_\rho^{(3)} &= (1+r)\frac{j\beta}{p_3}A_4 K_1(p_3\rho) & \text{if } \rho > b \end{cases} \tag{2.35}$$

$$H_\phi(\rho,\phi,z=0^-) \approx \begin{cases} H_\phi^{(1)} &= (1-r)\frac{j\omega\epsilon_1}{p_1}A_1 I_1(p_1\rho) & \text{if } \rho < a \\ H_\phi^{(2)} &= (1-r)\frac{j\omega\epsilon_2}{p_2}[A_2 I_1(p_2\rho) - A_3 K_1(p_2\rho)] & \text{if } a<\rho<b \\ H_\phi^{(3)} &= (1-r)\frac{-j\omega\epsilon_3}{p_3}A_4 K_1(p_3\rho) & \text{if } \rho > b \end{cases} \tag{2.36}$$

Where I_n and K_n are the modified Bessel function of the first and second kind of order n and $p_i = \sqrt{\beta^2 - \omega^2\mu_0\omega_i}$, where $i = 1, 2, 3$. Also μ_0 is the permeability of free space, ϵ_i is the permittivity of each region, r is the reflection coefficients of the field amplitude. Assuming an arbitrary value for one of these coefficients will determine the other three via matching the boundary conditions [47].

The propagation constant β for the fields in this structure can be found via dispersion relation:

$$AB - CD = 0, \tag{2.37}$$

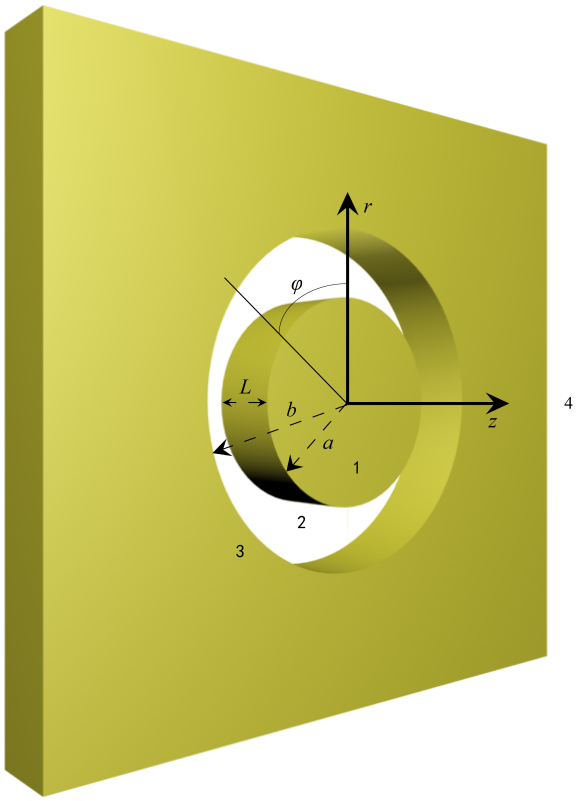

Figure 2.3: Schematic view of an coaxial aperture. The regions 1, 2, 3 and 4 has relative permittivity of ϵ_1, ϵ_2, ϵ_3 and ϵ_4 respectively.

where

$$A = \frac{I_0(p_2a)}{I_0(p_1a)} - \frac{\epsilon_2 p_1}{\epsilon_1 p_2}\frac{I_1(p_2a)}{I_1(p_1a)},$$

$$B = \frac{\epsilon_2 p_3}{\epsilon_3 p_2}\frac{K_1(p_2b)}{K_1(p_1b)} - \frac{K_0(p_2b)}{K_0(p_1b)},$$

$$C = \frac{K_0(p_2a)}{I_0(p_1a)} + \frac{\epsilon_2 p_1}{\epsilon_1 p_2}\frac{K_1(p_2a)}{I_1(p_1a)},$$

$$D = -\frac{\epsilon_2 p_3}{\epsilon_3 p_2}\frac{I_1(p_2b)}{K_1(p_3b)} - \frac{I_0(p_2b)}{K_0(p_3b)}$$

Here the propagation constant β is function of frequency, permittivity of the regions at each frequency and geometry of structure, a and b.

The modes in region $1, 2$ and 3, are expressed using modified Bessel functions I_n

and K_n, which are defined by the equivalent alternatives using Bessel function J_n as:

$$I_n(x) = i^{-n} J_n(ix), \tag{2.38}$$

$$K_n(x) = \pi/2 i^{-n} H_n^{(1)}(ix). \tag{2.39}$$

As in the coaxial aperture in real metal, there exists loss in each region, which means that, the dielectric constants and propagation constant are complex in all regions. Therefore I_n and K_n to are chosen to satisfy the radiation condition, instead of J_n and Y_n in PEC. of CSP is from [47].

2.4 Mode Matching Method

The theoretical approach in Chap. 4 and Chap. 5 is based on the mode matching method (MMM), which is usually used to analyze the electromagnetic energy and phase information when discontinuity of wave guides is encountered [46, 48]. Therefore it is useful to review this technique here. The basic idea for this work is that the field given by the sum of modes on one side of a boundary should match to the field given by the modes on the other side of the boundary via the BCs. The field is given by mode expansion in each region. The orthogonality relation is then used to isolate modes. In this section, the general expression of mode matching method is given.

Considering two region 1 and 2. There are a series of forward propagating modes $\vec{E}_0^{(1)}(x,y)e^{i\beta_0 z}$ and backward propagating modes $r_\nu \vec{E}_\nu^{(1)}(x,y)e^{-i\beta_\nu^{(1)} z}$ in region 1. Similarly, there are forward propagating waves $\vec{H}_0^{(1)}(x,y)e^{i\beta_0 z}$ and backward propagating modes $-r_\nu \vec{H}_\nu^{(1)}(x,y)e^{-i\beta_\nu^{(1)} z}$. Thus the modes can be expressed by a superposition of waves, as:

$$\vec{E}^{(1)} = \vec{E}_0^{(1)}(x,y)e^{i\beta_0 z} + \sum_\nu r_\nu \vec{E}_\nu^{(1)}(x,y)e^{-i\beta_\nu^{(1)} z} \tag{2.40}$$

$$\vec{H}^{(1)} = \vec{H}_0^{(1)}(x,y)e^{i\beta_0 z} - \sum_\nu r_\nu \vec{H}_\nu^{(1)}(x,y)e^{-i\beta_\nu^{(1)} z} \tag{2.41}$$

$$\vec{E}^{(2)} = \sum_\mu t_\mu \vec{E}_\mu^{(2)}(x,y)e^{i\beta_\mu^{(2)} z} \tag{2.42}$$

$$\vec{H}^{(2)} = \sum_{\mu} t_{\mu} \vec{H}^{(2)}_{\mu}(x,y) e^{i\beta^{(2)}_{\mu} z} \tag{2.43}$$

At $z = 0$,

$$\vec{E}^{(1)}_{||} = \vec{E}^{(2)}_{||} \tag{2.44}$$

$$\vec{H}^{(1)}_{||} = \vec{H}^{(2)}_{||} \tag{2.45}$$

$$\int\int \vec{E}^{(}1)_{||} \times \vec{H}^{(}2)_{\gamma||}\, dx\, dy = \int\int \vec{E}^{(}2)_{\gamma||} \times \vec{H}^{(}2)_{||}\, dx\, dy \tag{2.46}$$

$$\iint \vec{E}^{(2)}_{\mu||} \times \vec{H}^{(2)}_{\gamma||}\, \mathrm{d}x\, \mathrm{d}y = A_{\mu\gamma} = 0 \tag{2.47}$$

unless $\mu = \gamma$, when the result is $A_{\gamma\gamma}$.

Therefore the transmission coefficient is:

$$t_{\gamma} = \frac{\vec{E}^{(1)}_{||} \times \vec{H}^{(2)}_{\gamma||}\, \mathrm{d}x\, \mathrm{d}y}{A_{\gamma\gamma}} \tag{2.48}$$

Similarly,

$$\iint \vec{H}^{(1)}_{||} \times E^{(1)}_{\alpha||}\, \mathrm{d}x\, \mathrm{d}y = \iint \vec{H}^{(2)}_{||} \times E^{(1)}_{\alpha||}\, \mathrm{d}x\, \mathrm{d}y \tag{2.49}$$

$$\iint \vec{H}^{(1)}_{0||} \times \vec{E}^{(1)}_{\alpha||}\, \mathrm{d}x\, \mathrm{d}y = B_{0\alpha} = 0 \tag{2.50}$$

unless $\alpha = 0$, which is B_{00}.

$$-\sum_{\nu} r_{\nu} \iint \vec{H}^{(1)}_{\nu||} \times \vec{E}^{(1)}_{\alpha||}\, \mathrm{d}x\, \mathrm{d}y = -\sum_{\nu} r_{\nu} B_{\nu\alpha} = -r_{\alpha} B_{\alpha\alpha} \tag{2.51}$$

where $B_{\nu\alpha} = 0$, unless $\nu = \alpha$.

Add Eq. 2.50 and Eq. 2.51, we have:

$$\delta_{0\alpha} B_{0\alpha} - r_{\alpha} B_{\alpha\alpha} = \iint \sum_{\mu} t_{\mu} (H^{(2)}_{\mu||} \times E^{(2)}_{\alpha||})\, \mathrm{d}x\, \mathrm{d}y \tag{2.52}$$

Where $\delta_{0\alpha} = 0$, unless $\delta = 0$, with $\delta_{00} = 1$.

Substituting Eq. 2.48 into Eq. 2.52, we can solve for reflection coefficient r.

In the following, I give the explicit modes at the discontinuity of coaxial structure

to a dielectric material with finite radius c, which can contribute to our theoretical analysis when c goes to infinity.

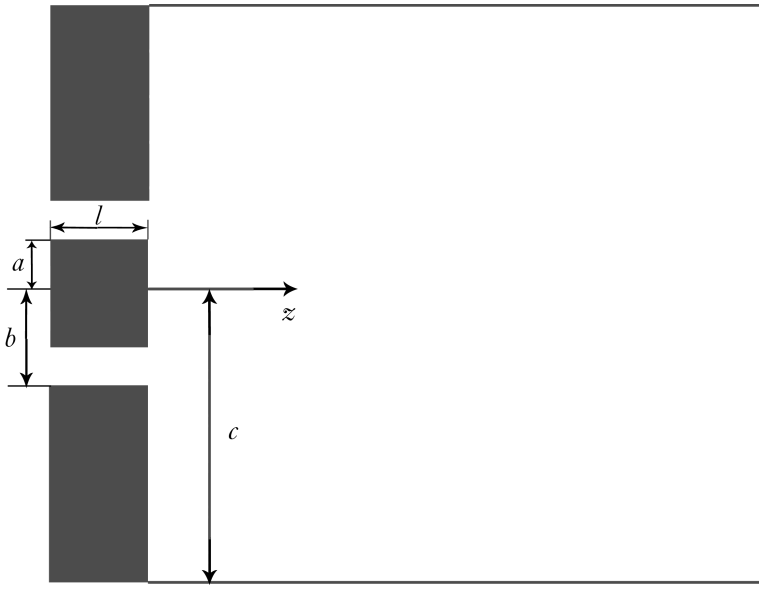

Figure 2.4: The coaxial aperture with inner radius a, outer radius b and length l is terminated at the right end ($z = 0$ plane), where a dielectric material with permittivity ϵ'_d extends to $\rho = c$ far.

Fig. 2.4 shows the coaxial aperture with inner radius a, outer radius b and length l, terminates at the right end ($z = 0$ plane), where the dielectric material with permittivity ϵ'_d extends to $\rho = 0$ far. The dielectric material inside the coax is assumed to have permittivity ϵ. The metal is assumed to be perfect conducting, and there's only mode inside the aperture, which means that, no electromagnetic waves extend into metal film. We consider TM mode here. First, in the coax the modes can be expressed by a superposition of TM modes, as:

$$E_\rho = \frac{1}{\rho} + \sum_\mu B_\mu [CJ_1(\mu\rho) + DY_1(\mu\rho)], \tag{2.53}$$

$$H_\phi = \sqrt{\frac{\epsilon_d \epsilon_0}{\mu_0}} \frac{1}{\rho} - \sum_\mu \frac{\omega\epsilon}{\beta} B_\mu [CJ_1(\mu\rho) + DY_1(\mu\rho)]. \tag{2.54}$$

The above two mode expressions are valid $a < \rho < b$.

The boundary conditions are:

$$E_z(\rho, \phi) = 0, \qquad \rho = a, b. \tag{2.55}$$

which gives the two equations:

$$CJ_1(\mu a) + DY_1(\mu a) = 0, \tag{2.56}$$

$$CJ_1(\mu b) + DY_1(\mu b) = 0. \tag{2.57}$$

Set the determinate of the above two linear equations to zero, we have:

$$D = -\frac{J_1(\mu a) - J_1(\mu b)}{Y_1(\mu a) - Y_1(\mu b)}C. \tag{2.58}$$

D is known if we set $C = 1$. In the following derivation, we introduce $C = 1$ and the coefficients only remains B_μ and D.

While on the right side, the mode can be expressed by a superposition of TM modes of circular waveguide, as:

$$E_\rho = \sum_\nu A_\nu J_1(\nu\rho), \tag{2.59}$$

$$H_\phi = \sum_\nu \frac{\omega\epsilon}{\beta} A_\nu J_1(\nu\rho), \tag{2.60}$$

where $\mu^2 = k'^2 - \beta^2$ is the propagation constant in coaxial aperture, and $\nu^2 = k^2 - \beta^2$ is for the outside of coaxial aperture (the right sidein Fig. 2.4).

At $z = 0$, the transverse fields must be continuous, therefore we have:

$$E_\rho = \frac{1}{\rho} + \sum_\mu B_\mu[J_1(\mu\rho) + DY_1(\mu\rho)] = \sum_\nu A_\nu J_1(\nu\rho), \tag{2.61}$$

$$H_\phi = \sqrt{\frac{\epsilon_d\epsilon_0}{\mu_0}}\frac{1}{\rho} - \sum_\mu \frac{\omega\epsilon}{\beta} B_\mu[J_1(\mu\rho) + DY_1(\mu\rho)] = \sum_\nu \frac{\omega\epsilon}{\beta} A_\nu J_1(\nu\rho). \tag{2.62}$$

2.5 Single Mode Matching

In chapter 3 and chapter 4, to be analytical, we use single mode matching. For this case, we make the approximation that only a single mode describes the field in the guide. This can be used in the symmetric geometry of the subwavelength system, where a single mode dominates. There are some geometries with which the single

mode matching method has been validated, such as single slit in real metal, double slits in PEC, and cylindrical nanorod in noble metal [2, 3, 49, 5]. Fig. 2.5 gives the example of past work using single mode matching method. In the subwavelength regime, a single mode dominates the behavior, which is the same case in our work. Thus, it allows a closed-form calculation of the reflection and transmission coefficients. Here I list some other work which utilize the single mode matching method.

Gordon in his work [49], considers only the lowest order TM modes of a subwavelength slit in real metal. The electric field in the freespace is written as an infinite sum of plane waves with TM polarization (see Eq. 3 of [3]). The results differs from PEC case as the existence of surface plasmons. In [3], the angle-dependent transmission through a narrow slit in a thick PEC film is considered. The angle dependence, θ, is included in the reflection coefficient (therefore also in the transmittivity). Unlike our theory, the angle tuning of the Fabry-Perot resonances relies on the slit width, as the reflection coefficient is angle dependent. The transmission is in good quantitative agreement with the experiments [50]. Single mode matching theory also proved accurate in the double slit geometry [2]. In the PEC case, only the even mode of the double-slit system is considered for the TM mode. It is shown that near-field interference modifies the transmission through the double-slit system, and that this phenomenon does not require the existence of surface plasmons. In Ref. [5], the geometry chosen is a cylindrical metal wire, where the approximation of surface wave of the cylindrical metal wire is to neglect the higher-order reflected waves to the first order. The reflection from that theory coincides well with comprehensive numerical solutions. It was also shown that the phase of reflection has a profound influence on the Fabry-Perot resonances of the metal wire.

2.6 Aperture Theory and Extraordinary Optical Transmission

2.6.1 Recent Developments in Transmission Through Apertures

Since the discovery of extraordinary optical transmission (EOT)in 1998 [9], there has been an explosion of research on the transmission through subwavelength apertures in metal films. Ebbesen found that the arrays of subwavelength holes in a metal film

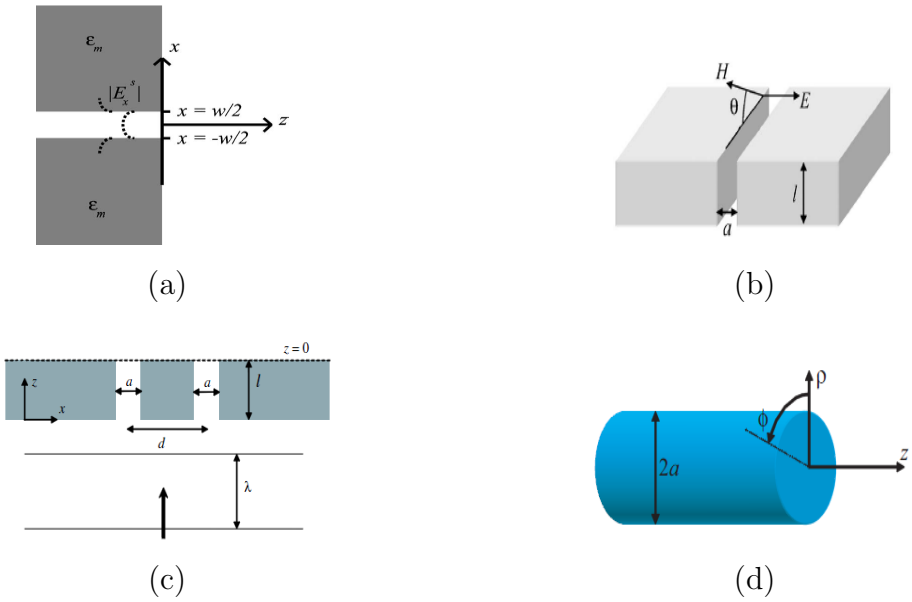

Figure 2.5: Past work using mode matching method. (a) The single slit [2] (b) Angle-dependent incidence of single slit [3] (c) The double slits [4] (d) Cylindrical nanorod [5]. All the slits are subwavelength dimensions.

exhibited much higher transmission than a single hole. It was further experimentally and theoretically proved that the shape of the aperture also strongly influenced the transmission [12, 10, 11]. Gordon explored the polarization dependence and the hole-shape dependence of the SP-enhanced transmission [11].

In 2001 Takakura proposed a structure of a linear slit in a metal [23]. He found that light transmission from a single slit was low in magnitude while resonance peaks of array were clearly observed, thus confirming that a grating acted as an amplifier (grating effect).

While linear slit only confine light in one dimension, it would further control over the lateral mode confinement and dispersion when the slit is bent into a circle. Baida [10] and Moreau *et al.* [51] proposed a structure of an array of annualar apertures which would exhibit a substantial incease in transmission compared with array of circular holes, which was demonstrated experimentally [21]. Lockyear *et al.* explored the resonant transmission of a single coaxial aperture in a thick metal [22], and they predicted the resonant frequency by ignoring end effects. They ascribed the discrepancy of theoretic prediction of resonant frequency from FEM simulations as Takakura-type shift [23],which means when the phase shift is not considered, the

Fabry-Perot resonance should be like:

$$f_{res} = \frac{c}{l}\frac{N}{2} \tag{2.63}$$

Baida [16] compared the cutoff wavelengths of propagative modes. The coaxial structure was found to exhibit large enhancements in transmission at wavelengths much longer than the usual cutoffs for cylindrical apertures. Haftel [15] and the coworkers attributed the enhancements to coupled cylindrical surface plasmons (CSP's) on the inner and outer surfaces of the aperture. CSP's are "launched" analogously to planar surface plasmons. Salvi et at. [14] used electron-beam lithography and gold liftoff to generate the 2D arrays of coaxial apertures in gold films on glass. They studied the transmission through an annular aperture array (AAA) structure in the visible range. However Haftel et al. [15] presented that the CSP peak would have been found in the near infrared range with the structure Salvi et al. presented in their work.

Burgos and coworkers [8] verified that certain metal/insulator/metal (MIM) waveguide geometries support negative-index modes in the visible. In their work [8], they reported a metamaterial composed of a single layer of coupled plasmonic coaxial waveguides in the blue spectral region.

While EOT was originally thought to ascribe to SPs [9, 52, 29], other investigations have shown that EOT can exit even for perfect conductors where SP's are absent [12, 11]. The results for the real metal differ significantly from the PEC due to the existence of surface plasmons, which can be exit when the real part of the relative permittivity dominates and it is negative [2]. Of the different geometries, the reason why the coaxial aperture has much higher transmission than others is due to the no-cutoff TEM mode, which can only be excited in coaxial structure if the illumination is on-axis and radially polarized. Surface plasmons are electron density waves at the surface of a metal. Above the plasma frequency, metals become transparent as they allow for EM wave propagation. At subwavelength regime, there exist extraordinary optical transmission, and surface plasmons are believed to play a vital role in the EOT. The explicit relationship are still under investigation. EOT doesn't necessarily require the existance of SPs, but SPs exist when real metal case is considered.

In a real metal, there is no TEM mode, so the lowest order radially polarized mode has a cut-off[53]. It has been shown that, the transmission of coaxial aperture can also be extraordinarily high if illuminated with linearly polarized light [51, 14]. The

TE_{11} mode is of particular importance as excitation of other modes is not possible with linearly-polarized plane wave at normal incidence. The higher order modes have larger cutoff wavelength and also the cutoff wavelength increases with the decrease of the aperture width.

2.7 Summary

Coaxial geometry is of interest for higher cut-off of lowest order mode, allowing for enhanced transmission. The phase and amplitude of reflection at the coax-ends had not been studied prior to this work, and play an important role on the FP resonances. There are many potential applications for these coaxial structures, such as optical sensing [39], optical trapping [54], metamaterials [8, 33], near-field spectroscopy [7, 28], and band-pass filter [40].

Chapter 3

Finite-difference Time-domain

3.1 Theory of Finite-difference Time-domain

In theory, Maxwell's equations can be used to determine the exact scattered field from any structure. However, for all but at few simple geometries, i.e., those that can be represented or conformally mapped into separable coordinate systems, closed form analytic solutions do not exist. This is due to the fact that in order to solve Maxwell's equations one must solve the complete electromagnetic boundary-value problem. That is to say, that the electromagnetic boundary conditions must be used to match tangential and normal field components at every point along a material discontinuity. In order for this to be performed analytically it must be done in a global fashion, so as to separate the independent variables and therefore allow for application of the boundary conditions. Unfortunately, this can only be done for a small number of geometries. Consequently, for complex geometries one must resort to numerical techniques, or computational electromagnetic methods (CEM).

During the last few decades several numerical electromagnetic techniques have been developed. Among these techniques are the finite element method (FEM), the boundary element method (BEM), the method of moments (MOM), finite-difference method (FDM), and the finite-difference time-domain method (FDTD). Each of these techniques has its own unique advantage, depending on the application at hand; however, by far the method receiving the most interest lately is the FDTD [55, 56].

In a unit cell of the Yee lattice, every E(H) component is centered in space and surrounded by four circulating H(E) components, simulating both the diferential and integral forms of Maxwell's equations. Field components are also centered in time (at

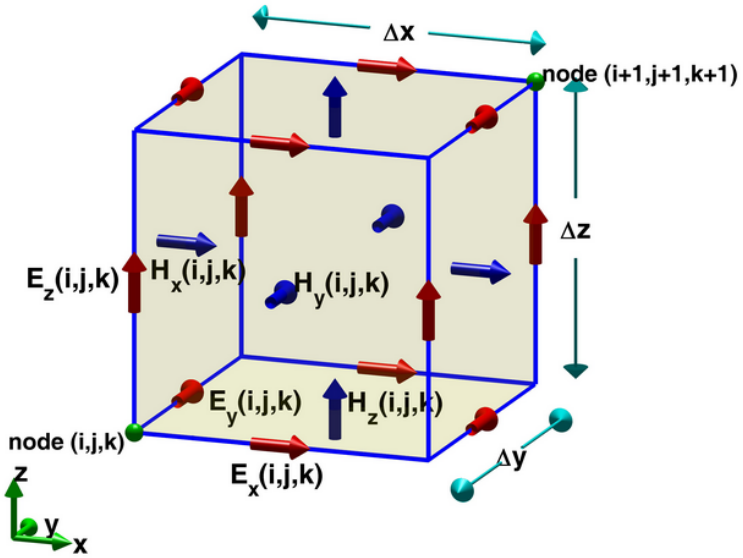

Figure 3.1: Three-dimensional FDTD lattics, the gray region applies to the two-dimensional lattice [6]. In a unit cell of the lattice, every $\mathbf{E}(\mathbf{H})$ component is centered in space and surrounded by four circulating $\mathbf{H}(\mathbf{E})$ components, simulating both the differential and integral forms of Maxwell's equations.

half time steps, labeled by n). Each field component (a small triangle) is determined from three previously computed ones which send arrows to it, forming a leapfrog pattern, e.g. , in the t-z plane:

Figure 3.2 shows that the field components are also centered in time, in a leapfrog pattern in the t-z plane.

Yee approximated the spatial and time derivatives using finite-difference expressions as follows

$$\frac{\partial u^n_{i,j,k}}{\partial x} = \frac{u^n_{i+1/2,j,k} - u^n_{i-1/2,j,k}}{\Delta x} + \mathcal{O}\left[(\Delta x)^2\right]$$
$$\frac{\partial u^n_{i,j,k}}{\partial t} = \frac{u^{n+1/2}_{i,j,k} - u^{n-1/2}_{i,j,k}}{\Delta x} + \mathcal{O}\left[(\Delta t)^2\right]$$

We note the $\pm 1/2$ increment in the i subscript of the x coordinate, as a finite-difference over $\pm 1/2\Delta x$. This notation makes the electric and magnetic fields interleaved in the space lattice at intervals $\pm\Delta x$.

Where the $\pm 1/2$ increments is in the n superscript (time coordinate) of u, denoting a time finite-difference over $\pm 1/2\Delta t$. Using these expressions, the electric and

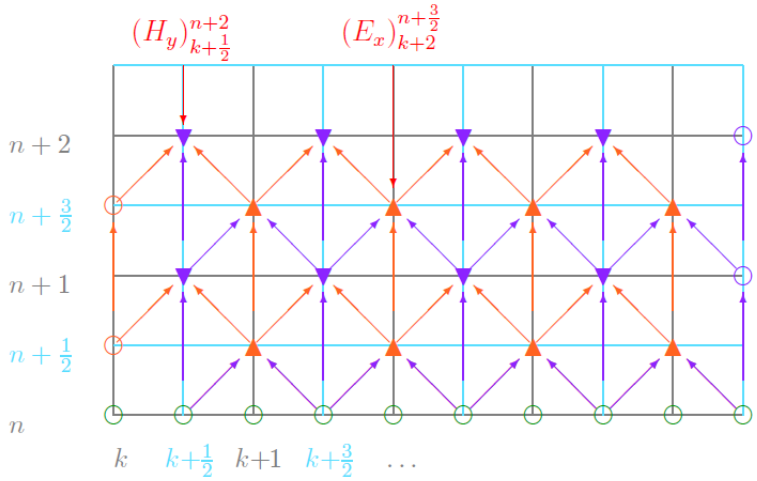

Figure 3.2: Field components are also centered in time, in a leapfrog pattern in the t-z plane.

magnetic fields are then calculated in time at intervals of $\pm 1/2\Delta t$ in accordance with the Yee algorithm.

Applying these, finite-difference approximations take the form

$$H_{i+1/2}^{n+1/2} = H_{i+1/2}^{n-1/2} - \frac{Q}{\mu_{i+1/2}}(\tilde{E}_{i+1}^{n} - \tilde{E}_{i}^{n}), \tag{3.1}$$

$$E_{i}^{n+1} = E_{i}^{n} - \frac{Q}{\epsilon_i}(H_{i+1/2}^{n+1/2} - H_{i-1/2}^{n+1/2}) \tag{3.2}$$

where $Q = \Delta t/(\sqrt{\epsilon_0\mu_0}\Delta x)$, $\tilde{E} = \sqrt{\epsilon_0/\mu_0}E$.

From the above expressions, it is found that the Yee algorithm has such attributes:

1. Central-difference in nature and 2nd-order accurate.
2. Solves for both electric and magnetic fields using Maxwell's curl equations — more robust than using either alone (accurate for a wider class of structures).
3. Satisfies the other two Maxwell's equations: $\nabla \times \vec{E}(\vec{H}) = 0$.
4. No need to enforce continuity condition at material interface. Simply specify $\varepsilon_{i,j,k}$ and $\mu_{i,j,k}$ at each location.
5. The explicit leapfrog time-stepping avoids using simultaneous equations and matrix inversion.

In open space problems, the computational domain must be truncated to finite size and appropriate boundary conditions must be carefully chosen to simulate its extension to infinity. These are called absorbing boundary conditions (ABC), which work as if all waves are out-going and no reflections happen (at least they are suppressed to an acceptable level). The early ABCs are analytical ABCs, which construct certain operators which annihilate out-going wave solutions at the boundary. An alternative to analytical ABC is *perfectly matched layer* (PML), which terminates the boundary with a highly effective absorbing-material medium (Berenger in 1994) [57]. The PML is usually a few lattice cells thick. As it works for plane waves of arbitrary incidence, polarization and frequency, and also works for domains comprised of inhomogeneous, dispersive,anisotropic and even nonlinear media (impossible with analytic ABCs), PML is the most effective and widely-used ABCs in recent FDTD simulations.

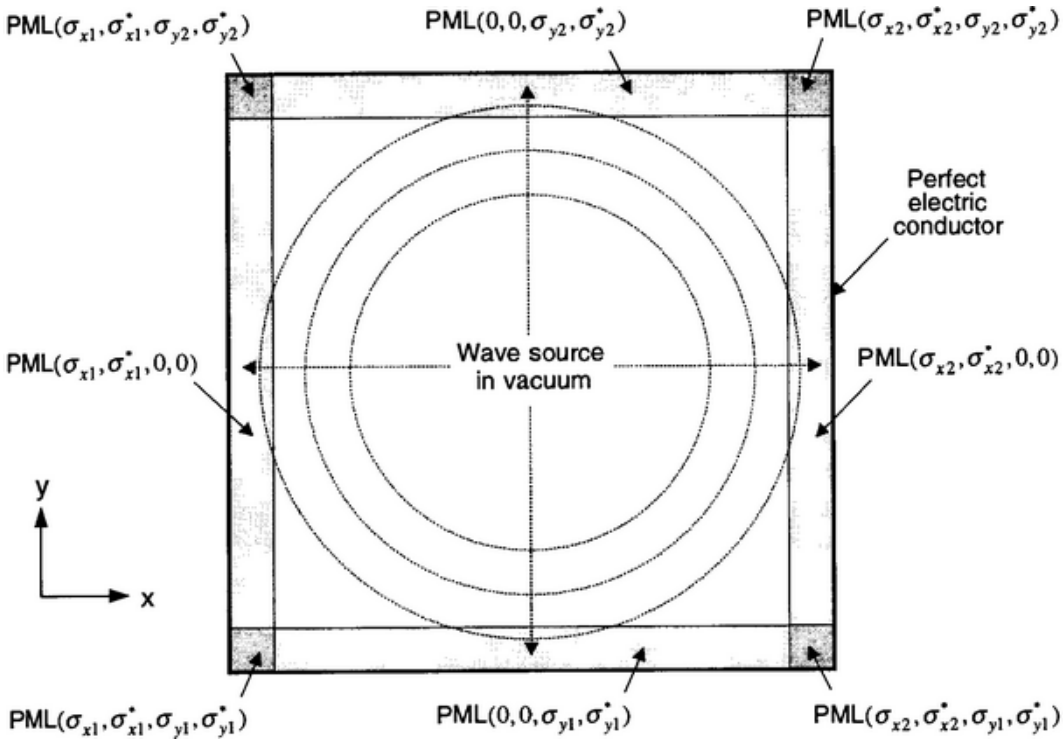

Figure 3.3: Figures show the finite size PMLs, the outer PECs/PMCs and choices of loss terms.

Figure 3.3 shows the finite size PMLs, the outer PECs/PMCs and choics of loss terms.

3.2 Work Using FDTD Simulations

3.2.1 Lumerical FDTD Solutions

FDTD Solutions from Lumerical Solutions, Inc. is high performance microscale optics simulation software using the FDTD method. It can simulate both $2D$ and $3D$ geometries. There are lots of advantages of the software compared to other FDTD solvers, such as: design parameterization and hierarchical layout via structure groups and analysis groups; support nonuniform mesh and automesh algorithms; simulation convergence autoshutoff; parallel computation on multi-core, multiprocessor; etc. Most of the FDTD simulation work was done using the $3D$ simulation software from Lumerical. Therefore we introduce some features in this chapter, including material database, boundary conditions, simulation objects, radiation sources, measurement monitors and parallel performance.

The Materials Database allows for the definition of complex materials using experimental data or parametrized models. The Material Explorer is used to check the material fits that will be used in the simulation, which uses a multipole dispersion model with coefficients determined by Lumerical's proprietary multi-coefficient fitting algorithm.

The simulation objects often refer to the modeled physical structure, as well as the simulation region which defines simulation parameters like the size, boundary conditions and mesh size. There are primitive shapes that make up all structure setups in FDTD, and preset structures and more complicated structure groups. We can also import structure data from other sources.

There are several boundary conditions supported by FDTD Solutions. Perfectly matched layer (PML) boundaries are most widely used boundaries in our work, which can absorb electromagnetic energy incident upon them. Metal boundary conditions are used to specify boundaries which are perfectly reflecting, allowing no energy to escape the simulation volume along that boundary. Periodic boundary conditions can

be used when both the structures and EM fields are periodic in one or more directions. Bloch boundary conditions can be used when the structures and the EM fields are periodic, but a phase shift exists between each period. Symmetric and asymmetric boundary conditions are used when when the geometry exhibits one or more planes of symmetry. Both the structure and source must be symmetric. Symmetric boundaries are mirrors for the electric field, and anti-mirrors for the magnetic field, while asymmetric boundaries are anti-mirrors for the electric field, and mirrors for the magnetic field. The easy way to decide whether symmetric or asymmetric boundary conditions are required, is that, the sources used must have the same symmetry as the boundary conditions.

We use PML boundaries. Symmetric boundary are also used as the coaxial structure is symmetric and source which we are using, dipole source polarized along z-axis or plane wave source normalized to the film, are symmetric. When computing the guided modes for the coaxial structure, the mode source is turned on. The following picture shows the geometry and boundary conditions we set up using plane wave source.

The mesh confinement is set to 'conformal variant 1' for gold, which gives more accurate results than staircasing, which gives numerical instability. The mesh we adopted on the surface of the ring is 1 nm, smaller than the mesh set of 2 nm used inside the ring.

3.2.2 MEEP

MEEP is a FDTD simulation software package developed at MIT. It can simulate in 1D, 2D, 3D, and cylindrical coordinates. It is predicted to work more accurately when simulating coaxial structures as it can use cylindrical coordinate while software package from Lumerical cannot.

In our work, we use the libctl/Scheme scripting interface to MEEP. The use of MEEP revolves around the control file, abbreviated "ctl" and is usually named as *name.ctl*, which is written in scripting language. The studied geometry, the boundary condition, the source properties, the output field, etc. are all specified in the ctl file. In MEEP, frequency is specified in units of $2\pi c$, which is equivalent to the inverse of vacuum wavelength. Absorbing boundaries in MEEP are handled by perfectly matched layers (PML). The finite thickness of the PML is important to reduce

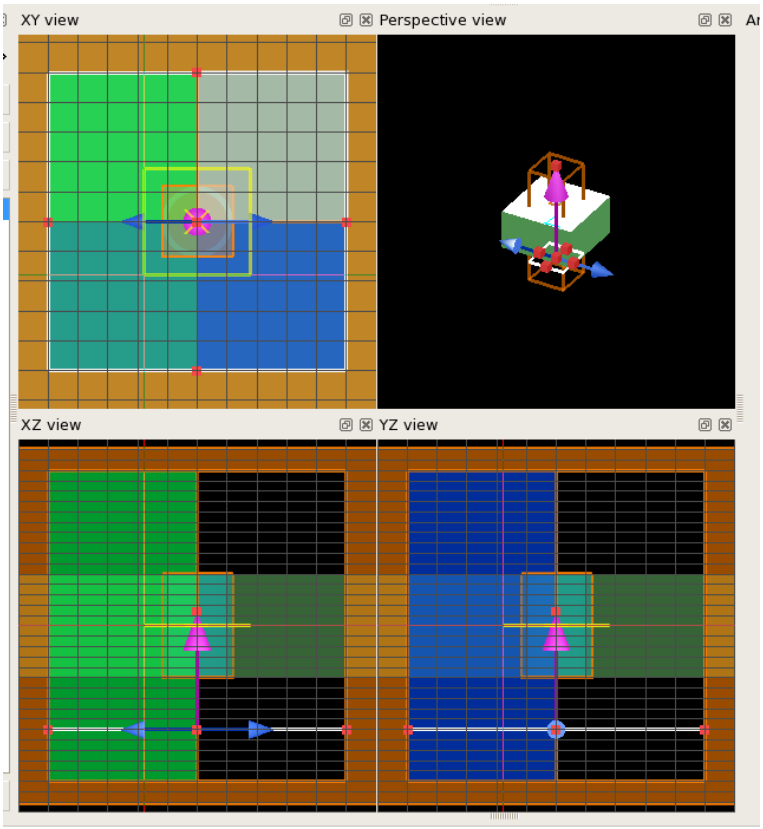

Figure 3.4: The geometry we setup to simulate our coaxial structure using Lumerical FDTD solutions. The right up one is the perspective view. The left up one is the top view. The lower two are side views. The dipole source is along the z-direction. The symmetry along x-axis and y-axis is used to reduce the computation domain to a quarter.

numerical reflections. A single variable, *resolution*, is used to discretize the structure of study in space and time, which gives the number of pixels per distance unit. The coaxial structure is specified by a *list* of geometric objects, stored in the *geometry* variable. As an example, we use

```
(set! geometry (list
(make block (center (/ sr 2) no-size 0 ) (size sr infinity l)
                    (material metal))
(make block (center (/ b 2) no-size 0) (size b infinity l) (material air))
  (make block (center (/ a 2) no-size 0) (size a infinity l) (material metal))
))
```

To specify the coaxial geometry.The full code can be found in the appendix.

The generated structure is shown as Fig. 3.5, where the black stands for high dielectric function material (metal) and white stands for air in our simulation.

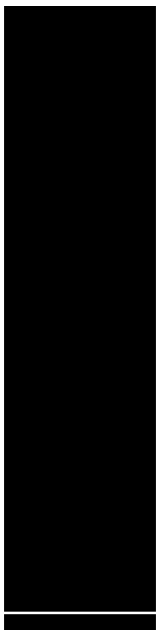

Figure 3.5: Dielectric function (black = high, white = air),for the coaxial structure with $a = 100$ nm, $b = 120$ nm.

Next step, we have to specify where we want MEEP to compute the flux spectra, and at what frequencies. (This must be done after specifying the geometry, sources, resolution, etc., because all of the field parameters are initialized when flux planes are created.)
For normalization purpose, we have to run the *ctl* file twice: one in free space without the *list* of geometric objects, and the other is with the coaixal geometries. We import these results Matlab (using its dlmread command).

To check whether the data is converged, we increased the resolution from 350 to 650, and reduced the cell size,to see by how much the numbers change. We can see steady blue shift of the transmission in Fig. 3.6. To ensure our accuracy of the convergence test, we compare the transmission spectrum from MEEP with the spectrum we get from Lumerical FDTD software package.

In Fig. 3.7, we simulated the same coaxial geometry as in MEEP. The difference is that, in MEEP we employed Gaussian source located at $z = -1000$ nm while in Lumerical software, we use a plane wave source positioned at $z = -500$ nm.

Although MEEP is more efficient due to the cylindrical coordinate system than

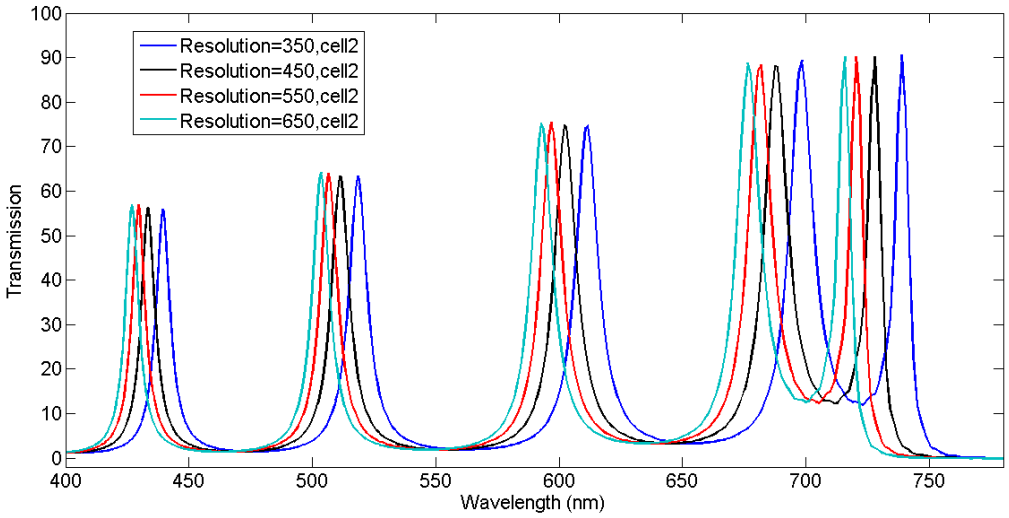

Figure 3.6: Transmission spectral of the coaxial structure from MEEP. The geometry is the same as in Fig. 3.5. Convergence is ensured by increasing the resolution and reducing the cell size.

Lumerical FDTD Solutions, Lumerical has the advantage of a easy-to-use graphical interface and a large database of material properties for real-metal cases.

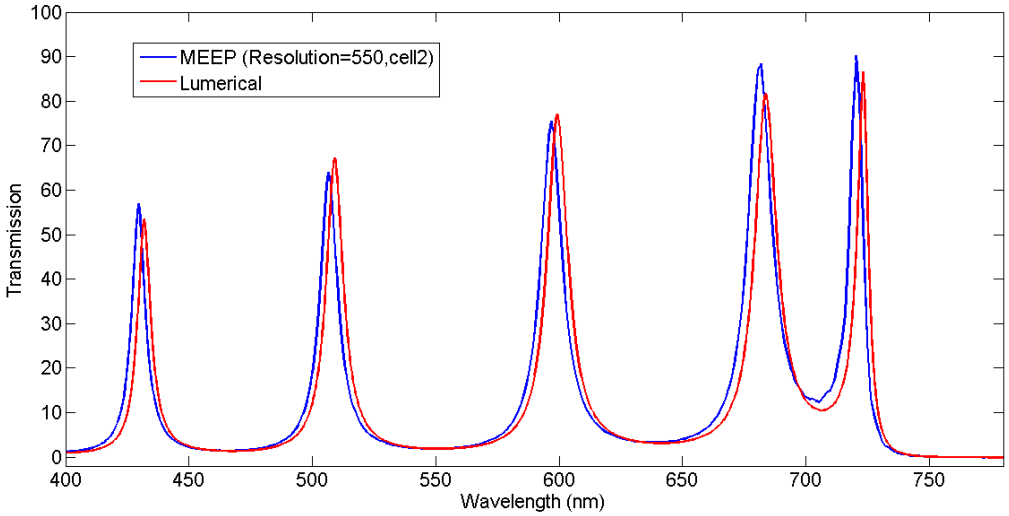

Figure 3.7: The same geometry as in Fig. 3.5. Blue curve: simulated by MEEP, with resolution 550 and cell size 2. Red curve: simulated by Lumerical FDTD Solutions. The plane wave source is at $z = -500$ nm.

Chapter 4

Electromagnetic transmission resonances for a single annular aperture in a metal plate

4.1 Introduction

In this chapter, the theory for reflection of the TEM mode at the end of an annular aperture in a metal plate is presented. This theory is accurate in the subwavelength regime, where the width of the slit significantly smaller than the wavelength, but is otherwise general. The theory shows quantitative agreement with comprehensive numerical FDTD simulations. It is seen from this theory that the phase and amplitude of reflection can vary significantly as the geometry and frequency change, and therefore, they are critical in the design of annular apertures in metal plates.

4.2 Theory of Reflection at the End of an Annular Aperture

Fig. 4.1 shows the annular geometry considered here, as well as the radially polarized lowest order mode. In the cylindrical coordinate system (ρ, ϕ, z), an annulus with inner radius a and outer radius b coaxial with the z-axis and the metal terminates at $z = 0$. The annulus is filled with dielectric with relative permittivity ϵ_d, and the metal is assumed to be a perfect electric conductor with thickness l.

The theory is based on matching the incident and reflected waves of a single

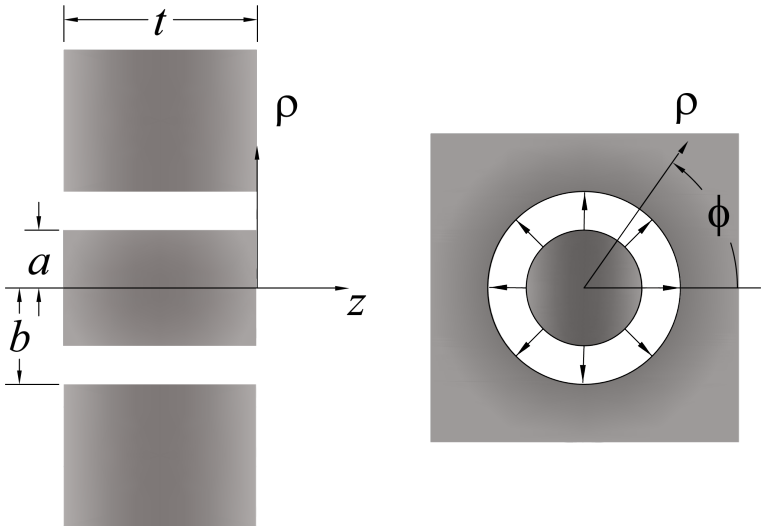

Figure 4.1: Schematic of annular aperture in a metal plate (i.e., a coaxial aperture). The electric field polarization of the TEM mode is also shown.

mode on one side of the boundary to the continuum of radiating and evanescent modes of free-space on the other side of the boundary, which is a dielectric with relative permittivity ϵ_d'. A similar approach has been used for slits [23, 2] and surface plasmons on cylindrical rods [58, 5]. Neglecting the higher order modes, the dominant single mode is the radially polarized TEM mode, which is confined in the annular region. The TEM mode propagates at arbitrary frequency, since it has no cutoff, with wavevector equal to the wavevector of a plane wave in the dielectric ϵ_d. The TEM electromagnetic field incident on the end of the metal can be normalized as:

$$E_\rho = \frac{e^{ik_d z}}{\rho}, \tag{4.1}$$

$$H_\phi = \sqrt{\frac{\epsilon_d \epsilon_0}{\mu_0}} \frac{e^{ik_d z}}{\rho}, \tag{4.2}$$

where $k_d = \omega\sqrt{\mu_0 \epsilon_0 \epsilon_d}$, ω is the angular frequency, and ϵ_0 and μ_0 are the free-space permittivity and permeability. The TEM mode is incident from $z = 0^-$ and we assume that the reflection is entirely into the same mode (traveling in the opposite direction). Therefore, for $a < \rho < b$, on the surface of the end where $z = 0^-$, the field

can be expressed as:

$$E_\rho(\rho,\phi,z=0^-) = (1+r)\frac{1}{\rho}, \tag{4.3}$$

$$H_\phi(\rho,\phi,z=0^-) = (1-r)\sqrt{\frac{\epsilon_0\epsilon_d}{\mu_0}}\frac{1}{\rho}. \tag{4.4}$$

where r is the reflection coefficient. The field is zero in the perfect electric conductor by definition.

For $z = 0^+$, the electromagnetic fields are expanded in terms of the free-space modes with the same rotational symmetry:

$$E_\rho(\rho,\phi,z=0^+) = \int_0^\infty t(k)\frac{\sqrt{k_0^2\epsilon_d' - k^2}}{\omega\epsilon_0\epsilon_d'}J_1(k\rho)dk, \tag{4.5}$$

$$H_\phi(\rho,\phi,z=0^+) = \int_0^\infty t(k)J_1(k\rho)dk, \tag{4.6}$$

where J_m is the Bessel function of the first kind of order m.

The transverse components of the electric and magnetic fields are continuous across the boundary; however, in this truncated (single) mode expansion, mode orthogonality on both sides of the boundary is used to determine r. The first orthogonality relation uses the orthogonal representation of the magnetic field in the $z > 0$ region. Equating the expressions for the electric fields, Eq. (4.3) and (4.5), then multiplying both sides by $J_1(k'\rho)\rho$, which is the form of the magnetic field modes for $z > 0$ times the radial component, and integrating over ρ from 0 to ∞ gives:

$$t(k) = (1+r)\frac{[J_0(ka) - J_0(kb)]\omega\epsilon_0\epsilon_d'}{\sqrt{k_0^2\epsilon_d' - k^2}}, \tag{4.7}$$

where the orthogonality for Bessel functions was used:

$$\int_0^\infty \rho J_m(u\rho)J_m(v\rho)\mathrm{d}\rho = \frac{\delta(u-v)}{u}. \tag{4.8}$$

where δ is the delta function, which refers to the distribution:

$$\delta(x) = \begin{cases} +\infty & x = 0 \\ 0 & x \neq 0 \end{cases} \tag{4.9}$$

Similarly, we consider the magnetic field by equating Eqs. (4.4) and (4.6). The

orthogonality of the mode is used by multiplying both sides by $\frac{1}{\rho}$, the electric field shape for $z < 0$, times the radial coordinate ρ (i.e. $\frac{1}{\rho}\rho = 1$) and integrating over ρ from a to b. Using $t(k)$ from Eq. (4.7) gives:

$$r = \frac{1 - G}{1 + G}, \tag{4.10}$$

where G is:

$$G = \sqrt{\frac{\mu_0}{\epsilon_0 \epsilon_d}} \frac{\omega \epsilon_0 \epsilon'_d}{ln\frac{b}{a}} \int_0^\infty \frac{[J_0(ka) - J_0(kb)]^2}{k\sqrt{k_0^2 \epsilon'_d - k^2}} dk. \tag{4.11}$$

where ϵ_0 is the material dielectric constant in vacuum, ϵ_d is the material dielectric constant outside the coaxial structure. Eq. (4.11) can be integrated by standard means.

4.3 Fabry-Perot Resonances of Coax in Metal Slab

Fig. 4.2 shows the Fabry-Perot resonances calculated by comprehensive elecromagnetic simulations using FDTD in cylindrical coordinates [59] (we use MEEP for the PEC case). The convergence of the FDTD simulations for frequencies greater than $0.5c/l$ was ensured by variations to the grid size, perfectly match layer thickness, simulation region size and simulation time. The metal plate spanned from $z = -0.5l$ to $z = 0.5b$. A broadband electric dipole source polarized along z was placed along the z-axis at $z = -(l + 0.5b)$. The transmission intensity through the plane at $z = 0.5l$ was monitored. The transmission was normalized to the same source and monitor locations, but for an infinitely thick metal in the positive z-direction, so that no longitudinal Fabry-Perot resonances were present. The same transmission resonances were obtained for radially polarized ring sources placed in the middle of the slit at one end of the plate. All dielectric materials were assumed to be vacuum.

By considering other slit widths (not shown), the FDTD simulations show that Fabry-Perot resonances become sharper as the annular slit width is decreased. This shows that the reflection of the TEM mode increases as the slit is made narrower. The slit width also influences the frequency of the resonances, which is only dependent on the phase of reflection for the TEM mode since its wavevector (propagation constant) is independent of slit-width. Since the wavevector of the TEM mode is the same as free space, the changes in the amplitude and phase of reflection that modify the Fabry-Perot resonances is purely a geometric effect.

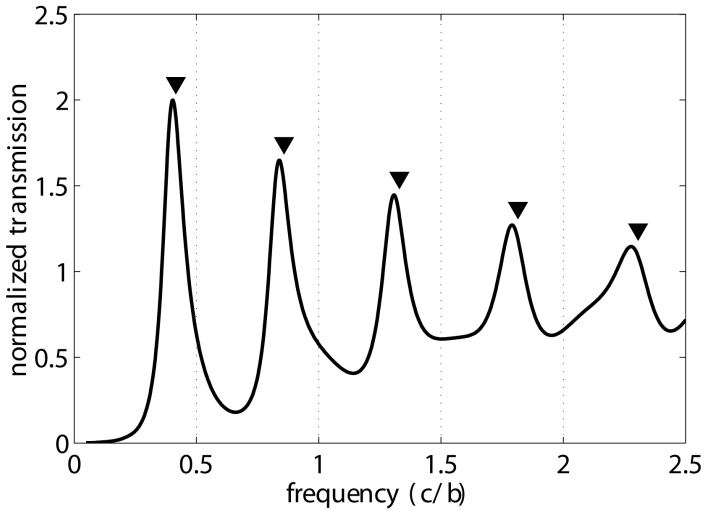

Figure 4.2: Electromagnetic transmission of a z-polarized dipole source and at distance $0.5b$ from the plate as measured through coaxial aperture, as calculated by FDTD. $a = 0.9b, b = l$. Normalized to the same source with a semi-infinite metal plate. Triangles show the frequency of resonances predicted by the analytic theory and using Eq. (4.12). Dotted vertical lines at frequency of 0.5, 1, 1.5, 2 and 2.5 c/b show the position of the resonances when neglecting the phase of reflection.

To compare the theory presented here with the FDTD simulations more quantitatively, the Fabry-Perot resonance condition is used. For $\epsilon_d, \epsilon'_d = 1$, the phase of reflection, ϕ_r, gives the frequency of the Fabry-Perot transmission resonances through:

$$f_{\text{res}} = \frac{c}{l}\left(\frac{N}{2} - \frac{\phi_r}{2\pi}\right) \tag{4.12}$$

where c is the speed of light in vacuum and N is the integer resonance number. Fig. 4.2 also shows, with triangles, the transmission resonance values predicted by the theory above, using Eq. (4.12). Reasonable agreement is seen between the resonant frequencies predicted the simple theory presented here and the comprehensive FDTD calculations. Small differences may be attributed to the truncation of higher order modes within the slit. For comparison, the resonance transmission peaks expected for the simplistic assumption that $\phi_r = 0$ are shown with dotted vertical lines. It is clear then that neglecting the phase of reflection gives a significant spurious offset in the resonance frequency.

Takakura shift means as in equation 4.12, when the phase shift is not considered,

the Fabry-Perot resonance should be like:

$$f_{\text{res}} = \frac{c}{l}\frac{N}{2} \tag{4.13}$$

Comparing equation 4.12 with equation 4.13, we can see their difference clearly. Our theory and simulation support the shift when considering the phase shift. We hope the experiment can revise the theory correctly.

Surface plasmons are electron density waves at the surface of a metal. Above the plasma frequency, metals become transparent as they allow for EM wave propagation. At subwavelength regime, there exist extraordinary optical transmission, and surface plasmons are believed to play a vital role in the EOT. The explicit relationship are still under investigation.

EOT doesn't necessarily require the existance of SPs, but SPs exist when real metal case is considered.

There exist some discrepancies between our simulation and the theory. The possible cause is that the ignored higher order modes still affect the transmission to some extend.

Fig. 4.4 using the infinitely long coaxial structure is used to normalize the transmission of the structure as in Fig. 4.3. It is also possible to estimate the reflectivity, $R = |r|^2$ from the FDTD simulations of the Fabry-Perot resonaces by comparing the maxima and minima in the transmission spectrum. For a Fabry-Perot with constant end-face reflection amplitude, the ratio between the maxima and the minima is given by:

$$M = \left(\frac{1+R}{1-R}\right)^2. \tag{4.14}$$

Fig. 4.5(a) shows the value of R calculated using FDTD and with the theory presented in this paper, for a thicker metal plate, $l = 4b$, to allow for closer resonances. Good agreement is seen between the theory and simulations for high frequencies. For lower frequencies, the FDTD is less accurate, which is due to the finite grid size and the subwavelength features. Furthermore, this is the regime where the approximation made in our theory is most valid. Therefore, we believe that the theoretical values may be more accurate than the numerical calculations in this regime. Fig. 4.5(a) shows oscillations in the reflectivity with variations in the frequency.

Figure 4.5 shows the reflection amplitude extracted from FDTD calculated transmission, compared with reflection calculated from analytic theory of Eqs. (4.10) and

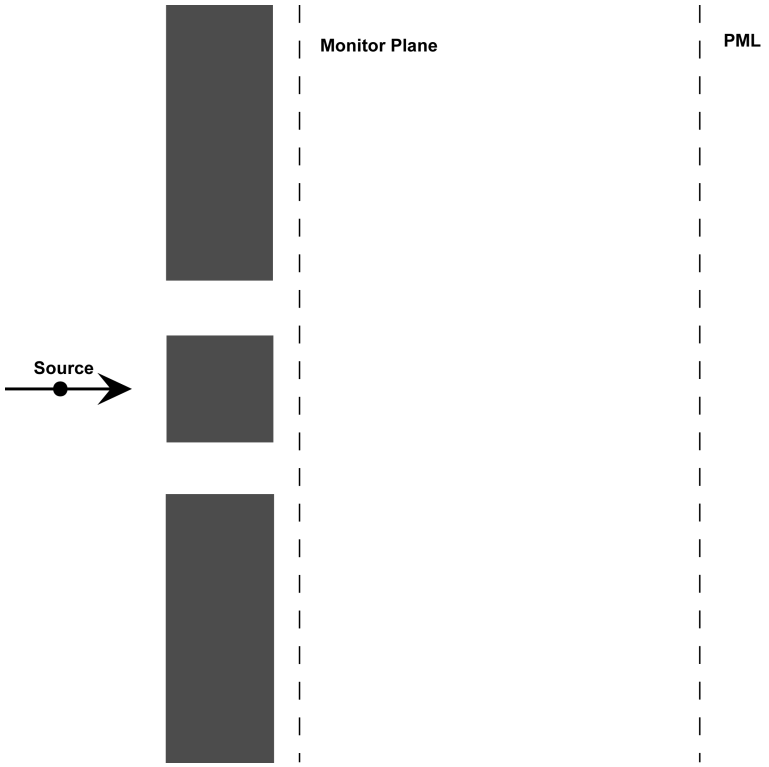

Figure 4.3: Left: the simulated structure is surrounded by PML (not shown in the picture). The monitor is positioned at the right end surface ($z = 0$ plane). Right: the infinitely long coaxial structure is used to normalize the transmission. PML cuts through the coax structure at far field. The monitor is also positioned at $z = 0$ plane.

(4.11). Also shows the reflection phase showing oscillations.

The phase shift at the aperture arise from the round trip of the mode at the two end-faces of the aperture. Each round trip contribute to the phase shift $\delta\phi$, and there exist countless round trip at the two-end faces. Then we add all these trips together and using some algebra, we get the expression for the phase shift between the two end-faces.

Fig. 4.5(b) shows the phase of reflection calculated by the theory (and already compared with FDTD in Fig. 4.2). This figure is shown in order to demonstrate that oscillations are also seen in the phase of reflection. To understand better the oscillatory behavior, we consider the heart of the theory presented here, as represented by Eq. (4.11). This equation diverges when $k_0^2\epsilon'_d = k^2$. The value of the non-diverging part of the integrand at that point plays a dominant role in the integral itself. In particular, the value of $[J_0(ka) - J_0(kb)]^2$ at the singular point will give changes to both the phase and the amplitude, which produces the oscillations. The physical

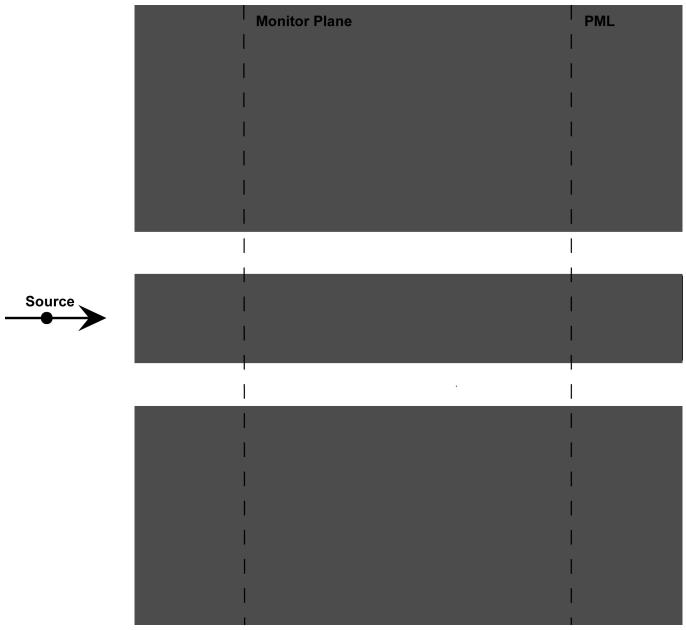

Figure 4.4: Left: the simulated structure is surrounded by PML (not shown in the picture). The monitor is positioned at the right end surface ($z = 0$ plane). Right: the infinitely long coaxial structure is used to normalize the transmission. PML cuts through the coax structure at far field. The monitor is also positioned at $z = 0$ plane.

interpretation here is that there are radially transverse resonances at the ends of the annular aperture that correspond to waves traveling radially out along the metal surface at the ends of the aperture and interfering constructively or destructively to modify the reflection. A similar behavior has been seen for the double slit in a perfect metal [4]; however, here it is seen for a single annular slit only.

The transverse resonances and the radial nature of the TEM modes are two key differences between the theory presented here and the equivalent theory for a single linear slit in a metal film [23, 3]. The linear and the annular slit theories should give equivalent results in the limit of a very wide radius, which we show in the following discussion. For a narrow annular slit ($b \approx a$), with $\epsilon_d = \epsilon'_d = 1$, Eq. (4.11) becomes:

$$G = \frac{a}{b-a} \int_0^\infty \frac{[J_0(ka) - J_0(kb)]^2}{k\sqrt{1 - (\frac{k}{k_0})^2}} dk. \tag{4.15}$$

For fixed m and $|x| \to \infty$, $J_m(x) \to (\frac{2}{\pi x})^{\frac{1}{2}} \cos(x - \frac{mx}{2} - \frac{\pi}{4})$. We introduce $u = \frac{k}{k_0}$

here, after some algebra, G can be expressed as:

$$G \to \frac{a}{b-a}\int_0^\infty \frac{4\sin^2\left[\frac{k_0 u(a-b)}{2}\right]}{\pi a k_0 u^2\sqrt{1-u^2}}du \tag{4.16}$$

Normalizing the slit-width dimension to wavelength $a' = \frac{b-a}{\lambda_0}$:

$$G \to \int_{-\infty}^{\infty} \frac{1}{\sqrt{1-u^2}}\frac{\sin^2(\pi u a')}{\pi^2 u^2 a'}du, \tag{4.17}$$

which is the same as Eq. (3) in Ref. [3].

This is expected since the annular slit of infinite radius is equivalent to a linear slit; that is, the curvature goes to zero, the radial polarization becomes linear TM locally and the transverse resonances of the annulus become negligible.

4.4 Conclusion

In summary, we have derived a theory for the reflection for an annular slit in a metal plate. The theory shows agreement with the Fabry-Perot resonances calculated by the comprehensive FDTD method for narrow slits. The theory shows the important role of transverse resonances in the annular slit system, which are not present in the simple linear slit. The theory is of interest to on-going studies of coaxial structures in metal films, which could impact many fields including near-field optics, optical sensing and metamaterials [33, 8].

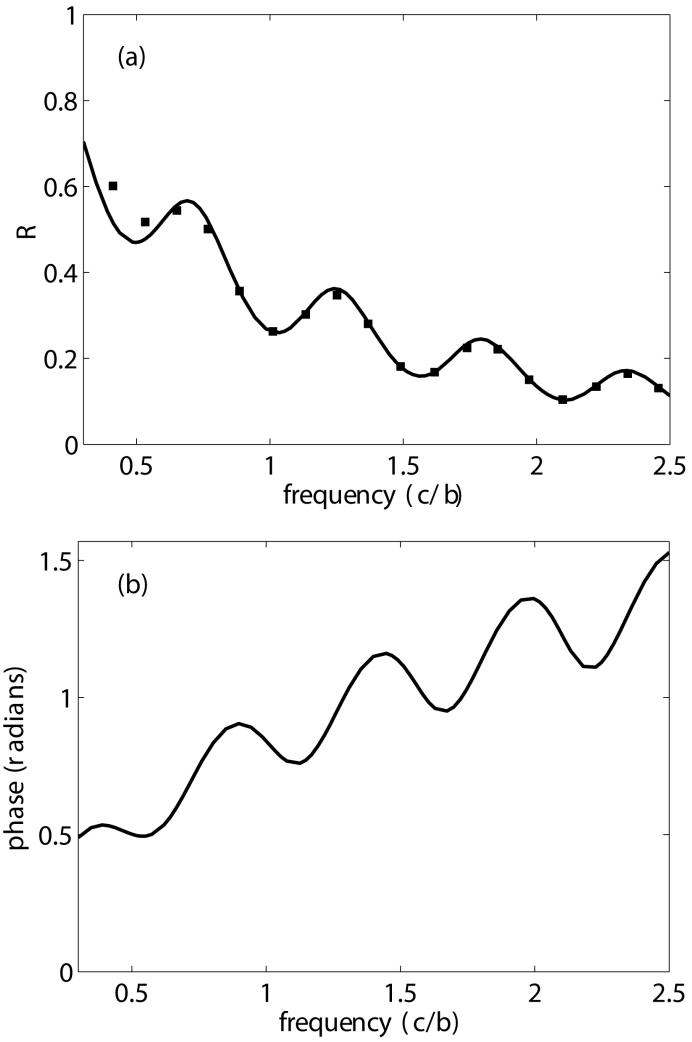

Figure 4.5: (a) Amplitude of reflection extracted from FDTD calculated transmission for $l = 4b$ and $a = 0.9b$, as compared with reflection calculated from the analytic theory of Eqs. (4.10) and (4.11). (b) Phase of reflection calculated by the analytic theory for $a = 0.9b$, showing oscillations.

Chapter 5

Tuning Plasmonic Resonance of an Annular Aperture in Metal Plate

The transmission theory of coax structure in real metal was proposed by Barmak Heshmat in Dr. Darcie's research group, and I contributed all of the FDTD simulation work.

5.1 Introduction

In this chapter, we present an analytic theory that accurately describes the reflection of the radial CSP mode within a coaxial geometry. The theory provides the reflection amplitude and phase of radially polarized surface plasmon waves from the end faces of an annular aperture in a plate made of a real material. Based on this theory, it is demonstrated that transverse resonances produce oscillations in the dependence of reflection amplitude and phase on the aperture geometry, which is of direct relevance to the wavelength and quality of the plasmonic resonances. The theoretical approach is also used to tune apertures to a specific resonant transmission peak, as confirmed by comprehensive FDTD simulations.

5.2 Theory of end-face reflection from an annular aperture in a metal plate

The theoretical approach is based upon the single-mode-matching method, where a single mode within the waveguide region is matched to a continuum of radiation and

evanescent modes to obtain the reflection properties. With the reflection coefficient and the mode's propagation constant, the wavelength and quality of the localized resonances can be obtained using Fabry-Perot theory. This method is accurate for subwavelength systems where the single-mode approximation represents the field distribution well. It has been applied successfully to the reflection from an annulus in a perfect electric conductor [43] and a number of other systems including subwavelength slits [23, 4], and surface plasmons at a step-edge [49, 58].

For $z = 0^+$, the electric and magnetic fields are expanded in terms of a continuum of modes with the same symmetry as the CSP:

$$E_\rho(\rho, \phi, z = 0^+) = \int_0^\infty t(k) \frac{\sqrt{\omega_0^2 \mu_0 \epsilon_3 - k^2}}{\omega \epsilon_3} J_1(k\rho) dk \tag{5.1}$$

and

$$H_\rho(\rho, \phi, z = 0^+) = \int_0^\infty t(k) J_1(k\rho) dk, \tag{5.2}$$

In these equations, $t(k)$ is a coefficient to be found and $J_1(k\rho)$ is the first order Bessel function of the first kind. Obviously, were we to assume a different material for $z > 0$, merely $\epsilon_4 \neq \epsilon_2$ in Eq. 5.

The transverse electric and magnetic fields are matched at $z = 0$, and the mode orthogonality relations are used to determine r. Eq. 1 is equated to Eq. 5 and both sides are multiplied by $J_1(k'r)r$ and integrated over ρ from 0 to ∞. Considering the orthogonality of the Bessel functions, this integration gives:

$$t(k) = (1 + r) \frac{\omega k \beta \epsilon_3}{\sqrt{\omega^2 \mu_0 \epsilon_3 - k^2}} [D_1(k) + D_2(k) + D_3(k) + D_4(k)] \tag{5.3}$$

with:

$$D_1(k) = \frac{-jA_1}{p_1(p_1^2 + k^2)} a \left(p_1 J_1(ka) I_2(p_1 a) + k J_2(ka) I_1(p_1 a)\right) \tag{5.4}$$

$$\begin{aligned} D_2(k) = \frac{-jA_2}{p_2(p_2^2 + k^2)} [b \left(p_2 J_1(kb) I_2(p_2 b) + k J_2(kb) I_1(p_2 b)\right) \\ - a \left(p_2 J_1(ka) I_2(p_2 a) + k J_2(ka) I_1(p_1 a)\right)] \end{aligned} \tag{5.5}$$

$$D_3(k) = \frac{jA_3}{p_2(p_2^2+k^2)}[b\,(kJ_2(kb)K_1(p_2b) - p_2J_1(kb)K_2(p_2b)) \\ - a\,(kJ_2(ka)K_1(p_2a) - p_2J_1(ka)K_2(p_2a))] \tag{5.6}$$

$$D_4(k) = \frac{-jA_4}{p_1(p_1^2+k^2)}b\,(kJ_2(kb)K_1(p_3b) - p_3J_1(ka)K_2(p_3b))\,. \tag{5.7}$$

Next, Eq.2 and 6 are equated, and both sides are multiplied by $\rho E_\rho(\rho,\phi,z = 0^-)/(1+r)$ in the related region and again integrated over ρ from 0 to ∞. This gives the reflection coefficient:

$$r = \frac{1-G}{1+G} \tag{5.8}$$

with:

$$G = \frac{\int_0^\infty \frac{k\beta\epsilon_3}{\sqrt{\omega^2\mu_0\epsilon_3-k^2}}[D_1(k)+D_2(k)+D_3(k)+D_4(k)]^2dk}{\frac{\epsilon_1A_1^2}{p_1^2}\int_0^a I_1^2(p_1\rho)\rho d\rho + \frac{\epsilon_2}{p_2^2}\int_a^b[A_2I_1(p_2\rho) - A_3K_1(p_2\rho)]^2\rho d\rho - \frac{\epsilon_3A_4^2}{p_3^2}\int_b^\infty K_1^2(p_3\rho)\rho d\rho} \tag{5.9}$$

In contrast to the PEC case, which involves only a single simple integral [43], the derivation and final formulation is considerably more elaborate. This is necessary, however, to capture the plasmonic dispersion and the finite penetration of the field into the metal. Nevertheless, the integrals in Eq. 5.9 converge and G can be calculated as a complex number to give the reflectivity ($|r|^2$) and reflection phase (ϕ).

The solution in Eq. 5.8 and Eq. 5.9 represent the main result of the mode matching theory in real metal case. It captures the amplitude and phase of reflection of the lowest order mode at the interface to free space (or uniform dielectric). This incorporates both the physical effects of mode-shape mismatch and impedance mismatch that lead to the reflection coefficient. The theory is limited to the subwavelength regime. For larger slit widths, where higher order radial modes are allowed to propagate, the theory will give inaccurate results and full numerical simulation will typically be required to capture the scattering of such a system. Furthermore, for large radii, higher order azimuthal modes may be allowed. This does not necessarily mean that the theory presented will not be invalid - so long as the rotational symmetry of the zeroth order mode is preserved, the theory presented here is valid for larger radii. The theory assumes that the plasmon mode is supported, as defined by the existence

of solution to Eq. 2.37.

5.3 Behavior of reflection coefficient

Having developed a theoretical expression for reflection, we proceed to evaluate the reflection amplitude and phase of various structures. Fig. 2 shows the calculated amplitude and phase at the end-face of an annular aperture in PEC case and real gold. The calculation is done for wavelength of 632.8 nm and a relative permittivity of $-11.694 + 1.225i$ in real case [60], with the dielectric medium having relative permittivity of 1. Two main features can be seen from this figure: that the amplitude and phase experience an offset when changing the slit width of the annulus $(b - a)$, and that there are oscillations with variation in the annulus radius.

The changes with slit width result from variations in coupling to the free space (or uniform dielectric) modes. Narrower slits have larger reflection amplitudes because of increased impedance mismatch and mode-shape mismatch (between the CSP mode in the slit and the continuum of propagating modes in the uniform dielectric) as the width is decreased. It is well known for gap plasmons that decreasing the distance between two metals can increase the propagation constant of the mode in the gap, and the same is true for the CSP here [26]. Furthermore, the narrower gap confines the electromagnetic energy to a subwavelength region.

The oscillatory behavior with changes in the annulus radius arises from transverse resonances. Such transverse resonances are not present for a single linear slit, but do arise for double slits, where the electromagnetic energy is scattered resonantly between the slits [4]. For the annulus here, the scattering occurs transversely between opposite sides. For a more mathematical description of this phenomenon, it is instructive to consider Eq. 5.9, for which the integrand diverges when $k^2 = \omega^2 \mu_0 \epsilon_4$. The integrand at this value of the wave-vector will play an important role in the value of r, and the oscillation arises from the oscillatory nature of the J Bessel functions with variations in the radius. It should be noted as well that the integrals in denominator have monotonic behavior with changes of radius because of the presence of modified Bessel functions.

Fig. 5.1 shows considerable differences between PEC case and real metal case, this

difference even increases more if the wavelength is closer to the plasmon resonance wavelength of the gold. For instance for the wavelength of 500 nm, the reflectivity is noticeably different − up to even double − as shown in Fig 3. For the wavelengths and geometries considered here, the reflection is larger for the PEC case; but this is not generally true. For instance, in case of a single slit, which can be considered as an annular aperture with the inner radius of infinity, higher reflectivity has been found in PEC compared to real metal case [2]. Close to zero outer radius, the PEC case approaches unity reflection because the field is confined to extreme subwavelength dimensions and therefore the mode-shape mismatch with free-space becomes infinite. For the real metal case, however, there is finite extension of the electric field into the metal, even for infinitesimal dimensions, and so the reflection amplitude remains below unity. The differences in the locations of the extrema in PEC and real metal case are also due to plasmonic effects. These differences increase from less than 20 nm in Fig. 2 to 40 nm in Fig. 3 by change of excitation wavelength from 632.8 nm to 500 nm.

The phase of reflection is also quantitatively different between the real metal and PEC cases, more than double in the graphs shown in Fig. 2 and 3. In the verbiage of microwave engineering, the increase in the phase of reflection can be thought of as coming from a more inductive termination waveguide. This is consistent with the interpretation that real metals can be thought of as inductive elements in the plasmonic regime [61]. As will be discussed in the next section, the resonant thickness of the metal plates will be considerably less for the real metal case than predicted by the PEC case, even after accounting for the differences in the propagation constant within the aperture.

5.4 Fabry-Perot Resonances

For a finite metal plate of thickness l, the CSP propagating inside the annular aperture will experience reflection at both end-faces. Fabry-Perot resonances arise from multiple reflections between the end-faces, depending on the phase of reflection, ϕ:

$$l = \frac{m\pi - \phi}{\beta} \tag{5.10}$$

where m is the integer order of the Fabry-Perot resonance and β is found from

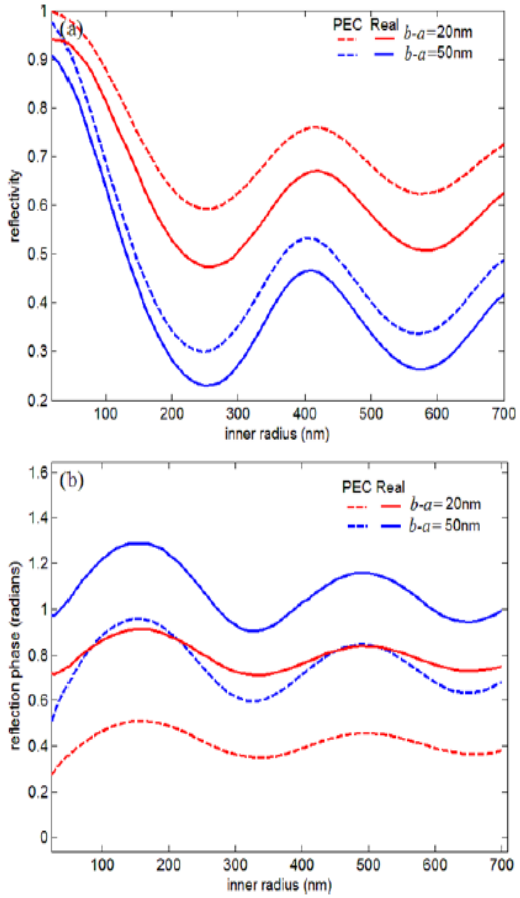

Figure 5.1: Evaluation of the theoretical reflection expression (Eq. 12) for annular apertures in gold plate at 632.8 nm free-space wavelength. The results are contrasted with PEC case in dashed lines. (a) the reflectivity and (b) phase of the reflection coefficient as function of inner radius, a, for slit widths $(b-a)$ of 20 nm and 50 nm.

Eq. 5.9.

Based on the results of Fig. 5.1 and Eq. 5.10, we designed several annular aperture geometries to all have a Fabry-Perot resonance at the same wavelength of 632.8 nm. The geometric parameters of each design were then simulated by FDTD (Lumerical Solutions Inc.). The metal plate spanned from $z = 0$ to $z = l$ nm, with l the thickness of the plate. A parametric dispersion model was used with gold permittivity set to $-11.694 + 1.225i$ at 632.8 nm [58] (the software uses a proprietary multi-coefficient model for extrapolating the permittivity in different wavelengths fitting the experimental data). A z-polarized broadband dipole source was located at $z = 100$ nm. The perfect matched layer (PML) boundary conditions were used for the computa-

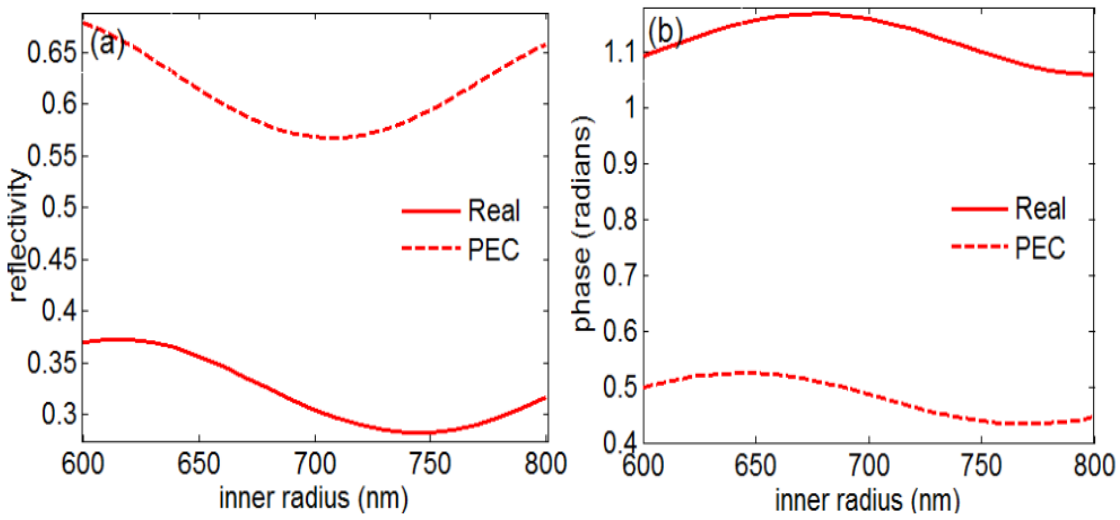

Figure 5.2: Difference between PEC case and real metal for annular aperture with slit size of 20 nm illuminated with 500 nm wavelength light. (a) reflectivity (b)phase.

tional domain, and the symmetric boundaries were adopted at x and y axis. A 1 nm mesh was set at both ends of the annular aperture and the mesh resolution was set to smaller than 2 nm inside the annulus. The convergence was ensured with variations of the simulation region size and simulation time.

Fig. 5.3 shows the results of the FDTD simulations for the various designs. Each case clearly shows a peak in the transmission through the aperture near the specified wavelength of 632.8 nm. The variations in the peak-widths and heights are expected from variations in the reflection amplitude and the propagation loss for the different geometries.

As it can be seen, by comparing Fig. 5.3 (a) and (b), the quality of the frequency profile of the resonance not only changes with a but also with slit size $(b-a)$. This is a direct effect of propagation constant and reflection amplitude being functions of a and b as stated in Eqs. 3, 4 and 12, and shown in Fig. 2. For example, the reflection amplitude for the red curve at inner radius of 50 nm is higher than reflection of green curve at inner radius of 250 nm (Fig. 2(a)), and this correlates with the higher quality resonance seen in Fig. 4(a). It can be inferred from Fig. 4(b) that change of slit size $(b-a)$ causes the relative value of peaks to be influenced. This is because the reflectivity in this case follows 50 nm curve in Fig. 2 (a), and therefore the variations

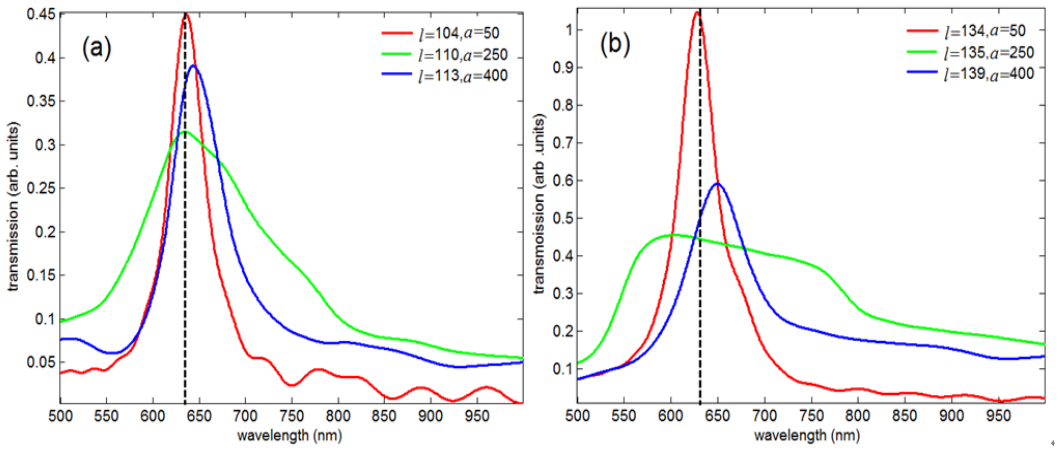

Figure 5.3: (a) Transmission in arbitrary units for $(b-a)$ value of 20 nm. Each curve relates to a different structure as specified in the legend and the dashed line is at 632.8 nm. In this figure a is the inner radius and l is the thickness of the plate (b) The $(b-a)$ value has been changed to 50 nm.

in reflection amplitude are more significant.

The good agreement of the resonances seen in the comprehensive electromagnetic simulations with the specified wavelength (632.8 nm) shows the predictive capability of the theory presented, which will be useful in future designs of apertures in metal films. Table 1 shows the wavelength at which the peaks arise from several additional simulations, all very close to 632.8 nm. Also, it is further evident from this table that the propagation constant inside the annulus obtained from finite-difference mode solver simulations match the calculated values of Eq. 3. This is because the effective refractive index obtained from the finite difference method agrees to that found by the calculation within 0.004 on average, showing that the simulations accurately capture the analytic CSP dispersion.

Figure 5.3 illustrates the changes of resonance wavelength with change of thickness. As can be seen, the resonance wavelength for the same order increases with thickness, and once again, good agreement is seen between our analytic method and FDTD simulations.

As the effect of inner and outer radius of the annular aperture was fully captured in reflection phase and amplitude, the effect of plate thickness l is important in tuning

Table 5.1: The effective refractive indexes and peak wavelength for geometries in Fig. 5.3, for structures designed to have peak at 632.8 nm.

a(nm)	b(nm)	l(nm)	n(analytic)	n(finite difference)	FP peak(nm)
50	100	124.23	1.7020	1.7067	634.03
50	100	310.12	1.7020	1.7038	636.20
50	100	496.02	1.7020	1.7004	638.73
250	300	135.38	1.5308	1.5600	611.85
250	300	342.06	1.5308	1.5407	629.39
250	300	548.75	1.5308	1.5361	634.39
400	450	139.04	1.5308	1.5202	649.23
400	450	345.72	1.5308	1.5243	643.42
400	450	552.41	1.5308	1.5262	640.96
50	70	104.42	2.3063	2.3029	639.83
50	70	241.61	2.3063	2.3029	639.83
50	70	378.80	2.3063	2.3046	639.10
250	270	110.81	2.1250	2.1403	638.00
250	270	259.71	2.1250	2.1354	640.56
250	270	408.60	2.1250	2.1334	641.66
400	420	113.44	2.1150	2.1177	647.56
400	420	263.04	2.1150	2.1204	645.89
400	420	416.64	2.1150	2.1177	647.56

the plasmonic resonances in such an aperture as well. This is attainable both with the Eq. 12 and 14 and FDTD approach. The analytic approach, however, can directly give the resonance thickness simply by substitution of phase in Eq.14. Unlike FDTD in which the thickness of the structure needs to be known prior to the simulation, the analytic approach can predict the thickness with a choice of a wavelength. This can serve as a prefabrication design guide for an intended wavelength of resonance.

Fig. 5.5 shows the distribution of the intensity of the electric-field in cross section of the annular aperture, when on resonance and when off resonance. For the on-resonance case, there is a nearly symmetric field distribution in the aperture (as expected from the Fabry-Perot resonance) and significant electric field intensity transmits through the aperture to the other side of the gold plate. For the off-resonance case, the electromagnetic energy does not build up within the aperture and significantly less transmission is observed.

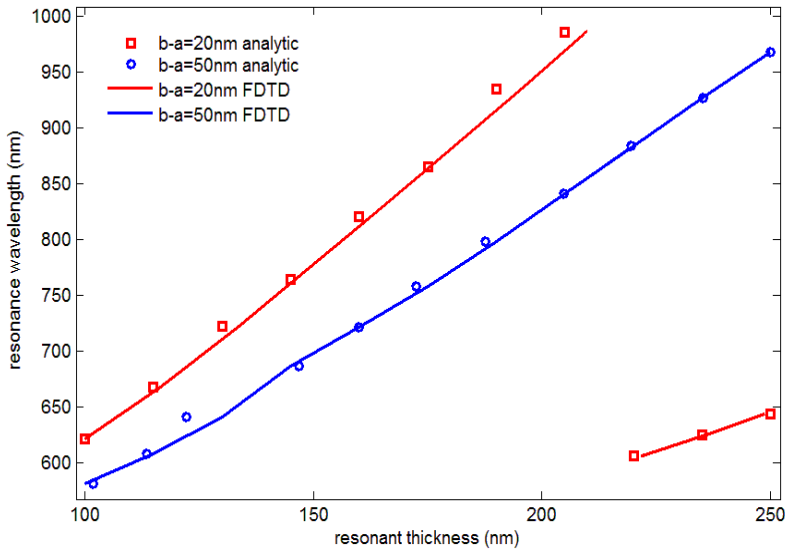

Figure 5.4: Variations of resonance wavelength with plate thickness l. The annular aperture inner radius is kept fixed at $a = 50$ nm.

Figure 5.5 shows the electric-field plot in $2 - D$, calculated by FDTD. The figure is the cross section of the annular aperture. The scalar bar is shown on the right.

5.5 Conclusion

We presented a theory for the end-face reflection of an annular aperture in a real metal. This theory is useful for determining the localized surface plasmon resonances associated with an annular aperture in a metal plate. Comparison with comprehensive FDTD simulations showed the good predictive design capability of the analytical approach and the results were contrasted with PEC case. The results presented in this work are relevant to annular apertures for use in metamaterials applications [8, 33], near-field optics [37], sensors [39, 35, 38, 36], and band-pass filters [40, 13]]. In particular, metamaterials based on annular structures rely on the plasmonic metal response to obtain interesting new physics, such as negative refractive index [8, 33]. However, in those works the important influence of the reflection remains elusive. This work represents an initial step towards a better understanding of the reflection properties in real metals for the annular geometry. For near-field optics applications, annular aperture resonances can boost the performance, for example, as found in a recent work involving Raman imaging [62]. Knowledge of the influence of real metals

is necessary to design near-field probes with the desired resonance wavelengths.

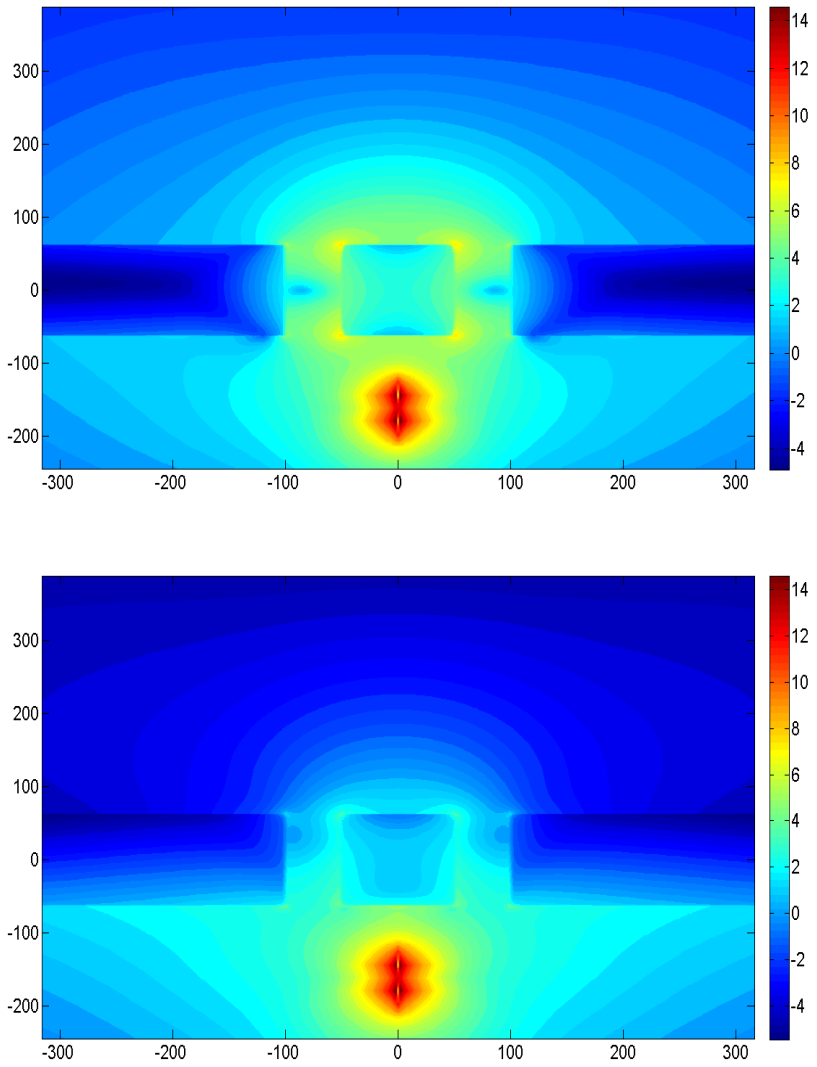

Figure 5.5: Electric-field plot in $2D$, calculated by FDTD. The figure shows the cross section of the annular aperture. (a) E-field at the resonance wavelength 632.8 nm (b) E-field at 500 nm wavelength. The scalar bar is shown on the right.

Chapter 6

Conclusions and Future Work

6.1 Summarization of our Findings

We study the resonance properties of a coaxial aperture in a PEC and in a real metal. For both cases, we present an analytic theory to describe the re ection properties of the aperture that agrees quantitatively with FDTD calculations. The reflection properties at the end-face are critical to determine both the wavelength and quality of Fabry-Perot resonant transmission from the CSP. The phase of reflection associated with the end-faces of a coaxial aperture affect the Fabry-Perot resonances seen at the microwave frequencies. The theory we developed in Chapter 3 and Chapter 4 can be applied to design coaxial apertures with desired resonance wavelength.

6.2 Applications of Coaxial Geometry

6.2.1 Filter Effect

Of all the subwavelength structure which exhibit EOT, hole arrays have always gained lots attention as it is higher transmission efficiency than linear slits. Baida proposed a coaxial aperture arrays in 2005 [14] which exhibit even higher transmission than hole arrays, and it has been proved by a lot of experiments [18, 17]. The shape of the hole also tremendously influences the transmission. The transmission of single annular aperture is of importance to realize the EOT of AAAs. At normal incidence, TEM mode is excited with frequencies dictated by the plate thickness and the radius of annulus. For non-normal incidence TE and TM modes are found [22]. Banzer [21] experimentally proved the enhancement in transmission through single coax was up

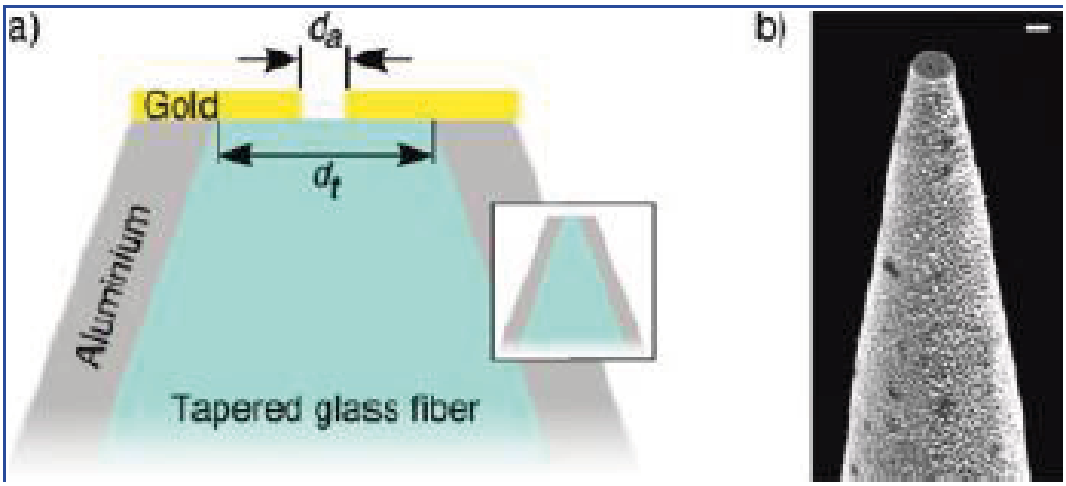

Figure 6.1: Schematic and SEM image of the EOT near-field fiber probe. (a) The fiber is tapered and then coated with an aluminum layer to prevent light leakage. The final taper diameter d_t determines the resonant TM mode cutoff-wavelength, by focused ion beam (FIB) milling. The aperture with diameter d_a is milled into a gold layer that is evaporated onto the end face. Inset: Conventional NSOM fiber. (b) The SEM image shows the final configuration with an aperture of diameter $d_a = 110nm$. The scale bar is $500nm$. The figure is from [7]

to four fold higher than through a hole aperture of the same radius. In this chapter it is exhibited that about 1000 times higher transmission could be achieved while the single hole aperture is replaced by coax. The gold permittivity function is taken from the paper of Johnson and Christy [60].

In Fig. 6.1, single coax of outer radius $100nm$, inner radius $50nm$, in a gold plate of $200nm$ thick. The dipole is positioned at z = $-200nm$, ρ from 0 to $150nm$. The coordinates are set the same as in the inset. In the inset of Fig. 6.1,single circular hole of radius $100nm$ embedded in the same gold plate. Dipole is positioned at z = $-200nm$, $\rho = 0$.

6.2.2 Near Field Optics

Figure 6.1 is the novel near field probe. Neumann et al. experimentally demonstrated such field probe facilitated by EOT [7]. Compared to conventional near field probes, EOT-facilitated probe exhibited 40× enhanced damage threshold and a 100× enhanced throughput. Figure 6.1 (from Neumann's work [7] shows the configuration of the probe. The comprehensive electromagnetic simulations confirmed that the high probe efficiency is facilitated by a new type of EOT that relies solely on the coupling

between the fiber waveguide at cutoff and the aperture. They experimentally show" that the spectral position of the resonance depends on the cutoff wavelength of the fiber waveguide, so that the peak wavelength could be tuned while maintaining the same aperture size".

6.2.3 Single annular aperture in sensors

A boost in the EOT through nanoscale apertures is of interest for applications in near-field optics. When nanoscale aperture structures embedded in real metal (usually gold, silver et. al noble metal), the SPPs coupling to the propagating modes largely enhance the local field intensity. The basic principle of single particle sensors is the exploitation of the fact that the spectral position of their resonances depends on the dielectric environment within the electromagnetic near field. Thus even molecular monolayers can lead to discernible spectral changes.

Fig. 6.2 shows a scanning electron microscope image of the preliminary coaxial aperture structure, as fabricated by focused ion beam milling (FIB). A coaxial shaped trench was milled into a gold film by a Strata Dual Beam DB235 SEM/FIB. SEM image shows the coaxial structure having inner radius 155 nm and outer radius 185 nm.

This aperture was designed to operate resonantly at 980 nm. We are presently performing spectroscopic characterization of that aperture; however, future experiments are planned to use this aperture in optical trapping experiments [54], as we have done in the past.

6.2.4 Negative-index Metamaterials

Metamaterials are artificial materials having some novel properties which don't exist in natural world. They determine their optical properties not by their chemical compositions, but by their subwavelength structure. Negative-index metamaterials (NIM) are a kind of metamaterials which exhibit 'left-handed' behaviour of light. The first fabricated NIMs were operated in the microwave regions, composed of split ring resonators and continuous wires [63]. With the improvement of fabrication technology, coaxial metal-insulator-metal (MIM) waveguides are observed to sustain modes of negative index when operating at the visible frequencies [8, 33]. Fig 6.3 shows the geometry of the negative-index metamaterial [8].

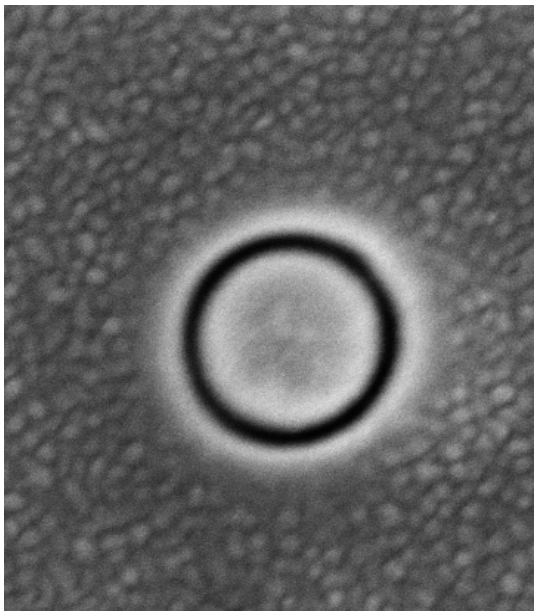

A

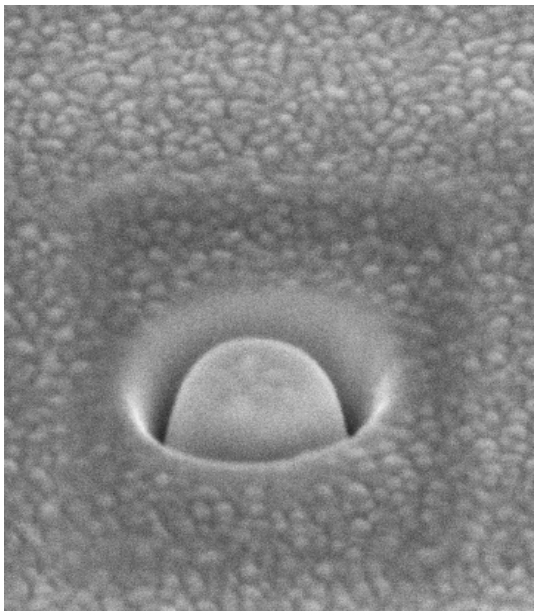

B

Figure 6.2: Scanning electron microscope image of the coaxial aperture in gold film taken from the FIB. The inner radius is 155 nm and outer radius is 185 nm. A: topview; B: 52° sideview.

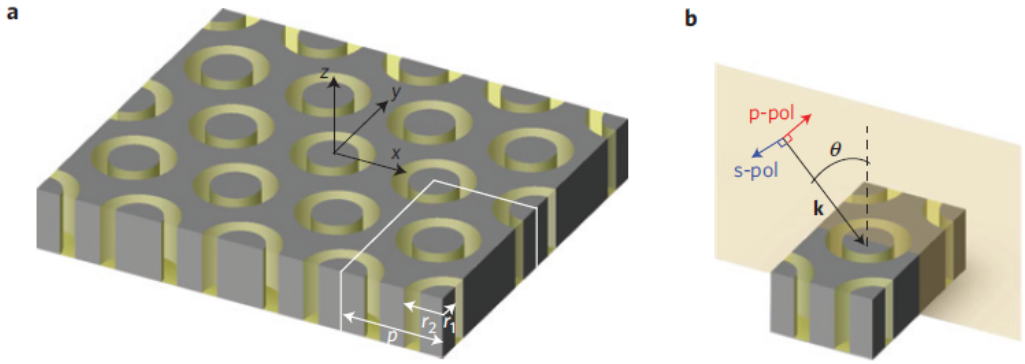

Figure 6.3: Negative-index metamaterial geometry (from [8]). a, Single-layer NIM slab consisting of a hexagonal array of subwavelength coaxial waveguide structures. The inner radius r_1, outer radius r_2 and array pitch p are defined in the image. b, Unit cell of the periodic structure. The angle-of-incidence θ is shown, as well as the in-plane ($p-$) and out-of-plane ($s-$) polarization directions associated with the incident wavevector k.

Bibliography

[1] V. M. Shalaev, "Ece 695s nanophotonics," 2006.

[2] R. Gordon, "Light in a subwavelength slit in a metal: Propagation and reflection," *Phys. Rev. B*, vol. 73, p. 153405, 2006.

[3] R. Gordon, "Angle-dependent optical transmission through a narrow slit in a thick metal film," *Phys. Rev. B*, vol. 75, p. 193401, 2007.

[4] R. Gordon, "Near-field interference in subwavelength double-slit in a perfect conductor," *Journal of Optics A*, vol. 8, pp. L1–L3, 2006.

[5] R. Gordon, "Reflection of cylindrical surface waves," *Opt. Express*, vol. 17, no. 21, pp. 18621–18629, 2009.

[6] D. W. Prather, "Advanced computational electromagnetics(lecture notes)."

[7] L. Neumann, Y. Pang, A. Houyou, M. L. Juan, R. Gordon, and N. F. van Hulst, "Extraordinary optical transmission brightens near-field fiber probe," *Nano Lett*, vol. 11(2), pp. 355–360, 2011.

[8] S. P. Burgos, R. deWaele, A. Polman, and H. A. Atwater, "A single-layer wide-angle negative-index metamaterial at visible frequencies," *Nature Materials*, vol. 9, pp. 407–412, 2010.

[9] T. W. Ebbesen, H. J. Lezec, H. F. Ghaemi, T. Thio, and P. A. Wolff, "Extraordinary optical transmission through sub-wavelength hole arrays," *Nature (London)*, vol. 391, pp. 667–669, 1998.

[10] F. I. Baida and D. V. Labeke, "Light transmission by subwavelength annular aperture arrays in metallic films," *Opt. Commun.*, vol. 209, pp. 17–22, 2002.

[11] R. Gordon, A. G. Brolo, A. McKinnon, A. Rajora, B. Leathem, and K. L. Kavanagh, "Strong polarization in the optical transmission through elliptical nanohole arrays," *Phys. Rev. Lett.*, vol. 92, p. 037401, 2004.

[12] K. J. K. Koerkamp, S. Enoch, F. B. Segerink, N. F. van Hulst, and L. Kuipers, "Strong influence of hole shape on extraordinary transmission through periodic arrays of subwavelength holes," *Phys. Rev. Lett.*, vol. 92, p. 183901, 2004.

[13] A. Roberts and R. C. McPhedran, "Bandpass grids with annular apertures," *IEEE Transactions on Antennas and Propagation*, vol. 36, pp. 607–611, 1988.

[14] J. Salvi, M. Roussey, F. I. Baida, M.-P. Bernal, A. Mussot, T. Sylvestre, H. Maillotte, D. V. Labeke, A. Perentes, I. Utke, C. Sandu, P. Hoffmann, and B. Dwir, "Annular aperture arrays: study in the visible region of the electromagnetic spectrum," *Opt. Lett.*, vol. 30, pp. 1611–1613, 2005.

[15] M. Haftel, C. Schlockermann, and G. Blumberg, "Enhanced transmission with coaxial nanoapertures: Role of cylindrical surface plasmons," *Phys. Rev. B*, vol. 74, p. 235405, 2006.

[16] F. I. Baida, A. Belkhir, D. V. Labeke, and O. Lamrous, "Subwavelength metallic coaxial waveguides in the optical range: Role of the plasmonic modes," *Phys. Rev. B*, vol. 74, p. 205419, 2006.

[17] Y. Poujet, J. Salvi, and F. I. Baida, "90% extraordinary optical transmission in the visible range through annular aperture metallic arrays," *Opt. Lett.*, vol. 32, pp. 2942–2944, 2007.

[18] S. M. Orbons, A. Roberts, D. Jamieson, M. I. Haftel, D. F. C. Schlockermann, and B. Luther-Davies, "Extraordinary optical transmission with coaxial apertures," *Appl. Phys. Lett.*, vol. 90, p. 251107, 2007.

[19] W. Fan, S. Zhang, B. Minhas, K. J. Malloy, and S. R. J. Brueck, "Enhanced infrared transmission through subwavelength coaxial metallic arrays," *Phys. Rev. Lett.*, vol. 94, p. 033902, 2005.

[20] J. Rybczynski, K. Kempa, A. Herczynski, Y. Wang, M. J. Naughton, Z. F. R. Z. P. Huang, D. Cai, and M. Giersig, "Subwavelength waveguide for visible light," *Appl. Phys. Lett.*, vol. 90, p. 021104, 2007.

[21] P. Banzer, J. Kindler, S. Quabis, U. Peschel, and G. Leuchs, "Extraordinary transmission through a single coaxial aperture in a thin metal film," *Opt. Express*, vol. 18, pp. 10896–10904, 2010.

[22] M. J. Lockyear, A. P. Hibbins, and J. R. Sambles, "Microwave transmission through a single subwavelength annular aperture in a metal plate," *Phys. Rev. Lett.*, vol. 94, p. 193902, 2005.

[23] Y. Takakura, "Optical resonance in a narrow slit in a thick metallic screen," *Phys. Rev. Lett.*, vol. 86, pp. 5601–5603, 2001.

[24] J. Wang, W. Zhou, and E. Li, "Enhancing the light transmission of plasmonic metamaterials through polygonal aperture arrays," *Opt. Express*, vol. 17, pp. 20349–20354, 2009.

[25] P. B. Catrysse and S. Fan, "Understanding the dispersion of coaxial plasmonic structures through a connection with the planar metal-insulator-metal geometry," *Appl. Phys. Lett.*, vol. 94, p. 231111, 2009.

[26] L. Novotny and C. Hafner, "Light propagation in a cylindrical waveguide with a complex, metallic, dielectric function," *Phys. Rev. E*, vol. 50, p. 4094C4106, 1994.

[27] F. I. Baida, Y. Poujet, J. Salvi, D. V. Labeke, and B. Guizal, "Extraordinary transmission beyond the cut-off through sub-k annular aperture arrays," *J. of Opt. Commun.*, vol. 282, p. 1463C1466, 2009.

[28] M. Walther, M. R. Freeman, and F. A. Hegmann, "Metal-wire terahertz time-domain spectroscopy," *Appl. Phys. Lett.*, vol. 87, p. 261107, 2005.

[29] I. B. H. Caglayan and E. Ozbay, "Extraordinary grating-coupled microwave transmission through a subwavelength annular aperture," *Opt. Express*, vol. 13, pp. 1666–1671, 2005.

[30] J. Zhang, S. Zhang, D. Li, A. Neumann, C. Hains, A. Frauenglass, and S. R. Brueck, "Infrared transmission resonances in double-layered, complementary-structure metallic gratings," *Opt. Express*, vol. 15, pp. 8737–8744, 2007.

[31] S. M. Orbons and A. Roberts, "Resonance and extraordinary transmission in annular aperture arrays," *Opt. Express*, vol. 14, pp. 12623–12628, 2006.

[32] S. M. Orbons, M. I. Haftel, C. Schlockermann, D. Freeman, M. Milicevic, T. J. Davis, B. Luther-Davies, D. N. Jamieson, and A. Roberts, "Dual resonance mechanisms facilitating enhanced optical transmission in coaxial waveguide arrays," *Opt. Lett.*, vol. 33, pp. 821–823, 2008.

[33] R. de Waele, S. P. Burgos, and A. Polman, "Negative refractive index in coaxial plasmon waveguides," *Opt. Express*, vol. 18, pp. 12770–12778, 2010.

[34] Q. Cao and J. Jahns, "Azimuthally polarized surface plasmons as effective terahertz waveguides," *Opt. Express*, vol. 13, p. 511C518, 2005.

[35] H. V. Chu, Y. Liu, Y. Huang, and Y. Zhao, "A high sensitive fiber sers probe based on silver nanorod arrays," *Opt. Express*, vol. 15, p. 12230C12239, 2007.

[36] K. A. Tetz, L. Pang, and Y. Fainman, "High-resolution surface plasmon resonance sensor based on linewidth-optimized nanohole array transmittance," *Opt. Lett.*, vol. 31, pp. 1528–1530, 2006.

[37] B. Hecht, B. Sick, and U. P. Wild, "Scanning near-field optical microscopy with aperture probes: Fundamentals and applications," *J. of Chem. Phys.*, vol. 112, pp. 7761–7774, 2000.

[38] R. Gordon, D. Sinton, K. L. Kavanagh, and A. G. Brolo, "A new generation of sensors based on extraordinary optical transmission," *Acc. Chem. Res.*, vol. 41, pp. 1049–1057, 2008.

[39] A. Brolo, R. Gordon, B. Leathem, and K. Kavanagh, "Surface plasmon sensor based on the enhanced light transmission through arrays of nanoholes in gold films," *Langmuir*, vol. 20, pp. 4813–4815, 2004.

[40] P. A. Krug, D. H. Dawes, R. C. McPhedran, W. Wright, J. C. Macfarlane, and L. B. Whitbourn, "Annular-slot arrays as far-infrared bandpass-filters," *Opt. Lett.*, vol. 14, pp. 931–933, 1989.

[41] J. R. Suckling, A. P. Hibbins, M. J. Lockyear, T. W. Preist, J. R. Sambles, and C. R. Lawrence, "Finite conductance governs the resonance transmission of thin metal slits at microwave frequencies," *Phys. Rev. Lett.*, vol. 92, p. 147401, 2004.

[42] P. Lalanne, J. P. Hugonin, and J. C. Rodier, "Theory of surface plasmon generation at nanoslit apertures," *Phys. Rev. Lett.*, vol. 95, p. 263902, 2005.

[43] D. Li and R. Gordon, "Electromagnetic transmission resonances for a single annular aperture in a metal plate," *Phys. Rev. A*, vol. 82, p. 041801, 2010.

[44] B. Heshmat, D. Li, T. E. Darcie, and R. Gordon, "Tuning plasmonic resonances of an annular aperture in metal plate," *Opt. E*, vol. 19 (7), pp. 5912–5923, 2011.

[45] D. Li, Y. Pang, and R. Gordon, "Design and fabrication of resonant coaxial nanoapertures in a gold film," *IEEE NANO*, 2011.

[46] J. D. Jackson, *Classical Electrodynamics Third Edition*. Wiley, third ed., August 1998.

[47] C. Yeh and F. I. Shimabukuro, *The Essence of Dielectric Waveguides*. Springer, 2007.

[48] A. Yariv and P. Yeh, *Photonics: Optical Electronics in Modern Communications, 6th ed.* Oxford University Press, 2007.

[49] R. Gordon, "Vectorial method for calculating the fresnel reflection of surface plasmon polaritons," *Phys. Rev. B*, vol. 74, p. 153417, 2006.

[50] J. R. Suckling, A. P. Hibbins, J. R. Sambles, and C. R. Lawrence, "Resonant transmission of microwaves through a finite length subwavelength metallic slit," *New J. Phys.*, vol. 7, p. 250, 2005.

[51] F. I. Baida, D. V. Labeke, G. Granet, A. Moreau, and A. Belkhir, "Origin of the super-enhanced light transmisssion through a 2-d metallic annular aperture array: a study of photonic bands," *Appl. Phys. B*, vol. 79, pp. 1–8, 2004.

[52] W. L. Barnes, W. A. Murray1, J. Dintinger, E. Devaux, and T. W. Ebbesen, "Surface plasmon polaritons and their role in the enhanced transmission of light through periodic arrays of subwavelength holes in a metal film," *Phys. Rev. Lett.*, vol. 92, p. 107401, 2004.

[53] D. M. Pozar, *Microwave Engineering, Third Edition*. Wiley, 1989.

[54] M. L. Juan, R. Gordon, Y. Pang, F. Eftekhari, and R. Quidant, "Self induced back-action optical trapping of dielectric nanoparticles," *Nature Physics*, vol. 5, pp. 915–919, 2009.

[55] A. Taflove and S. C. Hagness, *Computational Electrodynamics: The Finite-Difference Time-Domain Method, Third Edition*. Artech House Publishers, 3 ed., June 2005.

[56] R. Booton, *Computational Methods for Electromagnetics and Microwaves*. Wiley and Sons, Inc., New York, 1992.

[57] J. P. Berenger, "A perfectly matched layer for the absorption of electromagnetic waves," *J. Computational Physicas*, vol. 114, pp. 185–200, 1994.

[58] R. Kolesov, B. Grotz, G. Balasubramanian, R. J. Stöhr, A. A. L. Nicolet, P. R. Hemmer, F. Jelezko, and J. Wrachtrup, "Wave-particle duality of single surface plasmon polaritons," *Nat.Phys.*, vol. 5, pp. 470–474, 2009.

[59] A. F. Oskooi, D. Roundy, M. Ibanescu, P. Bermel, J. D. Joannopoulos, and S. G. Johnson, "A flexible free-software package for electromagnetic simulations by the fdtd method," *Comput. Phys. Commun.*, vol. 181, pp. 687–702, 2010.

[60] P. B. Johnson and R. W. Christy, "Optical constants of the noble metals," *Phys. Rev. B*, vol. 6, pp. 4370–4379, 1972.

[61] N. Engheta, "Circuits with light at nanoscales: optical nanocircuits inspired by metamaterials," *Science*, vol. 317, pp. 1698–1702, 2007.

[62] A. Weber-Bargioni, A. Schwartzberg, M. Cornaglia, A. I. J. J. Urban, Y. Pang, R. Gordon, J. Bokor, M. B. Salmeron, D. F. Ogletree, P. Ashby, S. Cabrini, and P. J. Schuck, "Hyperspectral nanoscale imaging on dielectric substrates with coaxial optical antenna scan probes," *Nano Lett*, 2011.

[63] D. R. Smith, W. J. Padilla, D. C. Vier, S. C. Nemat-Nasser, and S. Schultz, "Composite medium with simultaneously negative permeability and permittivity," *Phys. Rev. L*, vol. 84, pp. 4184–4187, 2000.

Appendix A

Additional Information

A.1 MEEP Code

```
{
(define-param a 0.10) ; inner radius
(define-param b 0.12) ; outer radius
(define-param pad 3) ; padding between waveguide and edge of PML
(define-param dpml 3) ; thickness of PML
(define-param l 1) ; length of simulation

(define sr (+ b pad dpml)) ; radial size (cell is from 0 to sr)
(define sl (+ l pad pad dpml dpml)) ; longitudinal size

(set! dimensions CYLINDRICAL)
(set! geometry-lattice (make lattice (size sr no-size sl)))

(set-param! m 0)

;(set! geometry (list
; (make block
;    (center (/ sr 2) no-size 0 ) (size sr infinity l) (material metal))
; (make block
;    (center (/ b 2) no-size 0) (size b infinity l) (material air))
; (make block
```

```
;    (center (/ a 2) no-size 0) (size a infinity l) (material metal))
;))


(set! pml-layers (list (make pml (thickness dpml))))
(set-param! resolution 150)

(define-param fcen 1.5) ; pulse center frequency
(define-param df 2.9)  ; pulse width (in frequency)
(set! sources (list
               (make source
                 (src (make gaussian-src (frequency fcen) (fwidth df)))
                 (component Er) (center 0 0 -1))))

(define-param nfreq 1000) ;number of frequencies at which to compute flux
(define trans ; transmitted flux
      (add-flux fcen df nfreq
                   (make flux-region
                    (center (/ (+ a b) 2) 0 (/ l 2))
                       (size (- b a) no-size no-size)
                   )))



(run-sources+ (stop-when-fields-decayed 50 Ez
           (vector3 0 0 (+(/ l 2) 0.5)) 1000)
           (at-beginning output-epsilon)
           (at-end output-efield-z))

(display-fluxes trans)
}
```

A.2 MAPLE Code

```
{
```

```
restart:with(plots):interface(showassumed=0):

G:=(mu/e)^(1/2)*(BesselJ(0,k*a)-BesselJ(0,k*b))^2/(k0^2*e1-k^2)^(1/2)/k*w*e0*e1;
i:=(BesselJ(0,t*a)-BesselJ(0,t*b))^2/t;c:=3e8;mu:=4*Pi*1e-7;
e0:=8.854187817e-12;e:=e0;w:=k0*c;G;k0=2*Pi/632.8*1e9;

g:=(mu/e)^(1/2)/(k0-k)^(1/2)*w*e0*e1;
s:=(BesselJ(0,k0*a)-BesselJ(0,k0*b))^2/(2*k0)^(1/2)/k0;
G1:=subs(k=kn*k0,e1=1,G); g1:=subs(k=kn*k0,e1=1,g);i1:=subs(e1=1,i);

 G1x:=-1/ln((a+x)/a)*(int(subs(b=a+x,G1*k0),kn=0.0..1.0-1e-3)
      +int(subs(b=a+x,G1*k0),kn=1.0+1e-3..infinity)
      +int(subs(b=a+x,g1*k0*s),kn=1.0-1e-3..1.0+1e-3)):

 ReG:=-1/ln((a+x)/a)*(int(subs(b=a+x,G1*k0),kn=0.0..1.0-1e-3)
     +int(subs(b=a+x,g1*k0*s),kn=1.0-1e-3..1.0)):


 A:=plot(subs(k0=2*Pi/632.8*1e9,x=50e-9,ReG),a=10e-9..700e-9); RE(G) 50nmthick

 ImG:=-1/ln((a+x)/a)*(int(subs(b=a+x,G1*k0),kn=1.0+1e-3..infinity)
      +int(subs(b=a+x,g1*k0*s),kn=1.0..1.0+1e-3)):

 A:=plot(subs(k0=2*Pi/632.8*1e9,x=50e-9,-I*ImG),a=10e-9..700e-9); IM(G) 50nmthick

 ReG:=-1/ln((a+x)/a)*(int(subs(b=a+x,G1*k0),kn=0.0..1.0-1e-3)
      +int(subs(b=a+x,g1*k0*s),kn=1.0-1e-3..1.0)):

 A:=plot(subs(k0=2*Pi/632.8*1e9,x=20e-9,ReG),a=10e-9..700e-9); RE(G) 20nmthick

 ImG:=-1/ln((a+x)/a)*(int(subs(b=a+x,G1*k0),kn=1.0+1e-3..infinity)
       +int(subs(b=a+x,g1*k0*s),kn=1.0..1.0+1e-3)):
 A:=plot(subs(k0=2*Pi/632.8*1e9,x=20e-9,-I*ImG),a=10e-9..700e-9); IM(G) 20nmthick
 }
```